Contributions to Mineralogy and Petrology (2022) 177:38
https://doi.org/10.1007/s00410-022-01900-1

ORIGINAL PAPER

Direct nanoscale observations of degassing-induced crystallisation in felsic magmas

Mattia Pistone[1] · Eric Formo[2] · Alan G. Whittington[3] · Thomas Herbst[4] · Elizabeth Cottrell[5]

Received: 2 June 2021 / Accepted: 4 February 2022 / Published online: 12 March 2022

Abstract

Water degassing plays a major role in magma transport and eruption by increasing liquidus temperatures, bubble and crystal volume fractions, and strongly affecting the viscosity of bulk magma. High spatial resolution textural analysis detailing the dynamics of bubble and crystal growth is key to unravelling the swift changes in magma crystallinity and gas content that affect the conditions of magma flow, fragmentation, and eruption. Ex situ observation of samples from a previous experimental study of magma degassing reveals that vesicles are surrounded by chemically heterogeneous residual glass that may be produced by newly formed minerals that are not observable at the microscale. Here, we present new in situ high-temperature (500–1100 °C), time-elapsed (every ~ 20 min at 200–800 °C, ~ 10 min at 900–1000 °C, and ~ 5 min at 1100 °C) observations of degassing of synthesised, hydrous (4.2 wt.% H_2O) dacite glasses using scanning transmission electron microscopy at 0.4 nm resolution. The experiments reproduce degassing of a silicic melt by high-temperature heated stage mounted in the analytical instrument. We monitor the dynamics of nucleation and growth of nanobubbles that experience coalescence and formation of microbubbles and trigger the nucleation and growth of nanolites of plagioclase, clinopyroxene, Fe-Ti oxides, and quartz, at the expense of the residual melt. The ability to image degassing and crystallisation at nanoscale reveals a sequence of complex physical and chemical changes of the residual melt and shows that the kinetics of crystallisation in silicic melts is modulated by the melt's ability to exsolve fluids that help form mineral nuclei and nanolites. Finally, we highlight that the competition between gas retention and crystallisation is initiated at the nanoscale and may anticipate the role of microlites in controlling rates of magma ascent in a volcanic conduit and modulating the style of the consequent volcanic eruption.

Keywords Degassing · Crystallisation · Nanolites · Magmas · Volcanic conduit

Introduction

Gas exsolution or degassing controls the ascent and eruption of magmas (e.g., Melnik and Sparks 1999; Barmin et al. 2002). Degassing produces gas bubbles that, if they are retained, can increase magma pressurisation (Sparks 1997; Girona et al. 2014), and facilitate magma flow if bubbles are deformable (at capillary number, $Ca > 1$; Llewellin et al. 2002; Llewellin and Manga 2005; Truby et al. 2015), which allow even near-solidus magma bodies to be extruded from the volcanic conduit (Swanson et al. 1989; Melnik and Sparks 1999; Pistone et al. 2012, 2013), or can increase magma viscosity if bubbles behave as rigid objects (at $Ca < 1$; Llewellin et al. 2002; Llewellin and Manga 2005; Truby et al. 2015). Vice versa, if sufficient gas release occurs through permeable pathways generated by bubble coalescence and fractures (e.g., Taisne and Jaupart 2008; Gaunt et al. 2014; Farquharson et al. 2016), magma depressurises

Communicated by Gordon Moore.

✉ Mattia Pistone
Mattia.Pistone@uga.edu

1 Department of Geology, University of Georgia, Franklin College of Arts and Sciences, Geography-Geology Building, 210 Field Street, Athens, GA 30602-2501, USA

2 Georgia Electron Microscopy Center, University of Georgia, Interdisciplinary STEM Research Building, 1, 302 East Campus Road, Athens, GA 30602, USA

3 Department of Earth and Planetary Sciences, The University of Texas at San Antonio, One UTSA Circle, San Antonio, TX 78249, USA

4 Department of Geological Sciences, University of Missouri, 101 Geological Sciences, Columbia, MO 65211-1380, USA

5 Department of Mineral Sciences, National Museum of Natural History, Smithsonian Institution, 10th Street and Constitution Avenue NW, Washington, DC 20560, USA

and can be erupted effusively or solidified at depth. Degassing also induces undercooling, where H_2O removal from the silicate melt increases its liquidus temperature and triggers crystallisation (e.g., Tuttle and Bowen 1958; Sparks and Pinkerton 1978; Cashman 1992; Johannes and Holtz, 1996; Hort 1998; Pistone et al. 2016a). The concomitant H_2O loss from the silicate melt and crystal nucleation and growth favors the increase of magma viscosity (e.g., Zhang et al. 2003; Ardia et al. 2008; 2014; Villeneuve et al. 2008; Hui et al. 2009; Whittington et al. 2009; Romine and Whittington 2015; Di Genova et al. 2017a).

Recent studies revealed that melt viscosity increase is initiated at the nanoscale when nanocrystals or nanolites (i.e., crystals of nanometre size; Sharp et al. 1996) are formed as a response to change in temperature (Mujin and Nakamura 2014; Di Genova et al. 2017a, 2018, 2020a, b; Mujin et al. 2017; Cáceres et al. 2020, 2021). In particular, the formation of Fe-Ti oxides drives Fe depletion in the residual melt (Di Genova et al. 2017a, 2018, 2020b), and H_2O loss by gas exsolution (Mujin et al. 2017; Di Genova et al. 2018) via heterogeneous bubble nucleation (Shea 2017; Cáceres et al. 2020), both of which favour a dramatic increase of melt viscosity by up to two orders of magnitude (Di Genova et al. 2017a, 2020b). Also, the effect of nanocrystallisation or "nanolitisation" (Di Genova et al. 2018) would favour an increase of magma viscosity as a consequence of the onset of strong particle–particle interactions at crystal contents as low as 10 vol.% (Di Genova et al. 2020a). In contrast, an exsolved gas phase has the potential to reduce magma viscosity dramatically (Pistone et al. 2012, 2013, 2016b). These recent studies focused on the formation of nanolites during relatively fast cooling (10 to 20 °C/s) of Fe-rich basaltic melts (Di Genova et al. 2017a, 2018, 2020b) and slow cooling (< 0.5 °C/s) of Fe-doped rhyolitic materials (Cáceres et al. 2020, 2021) from superliquidus temperatures. While these studies are relevant in highlighting the important role played by nanolites during crystallisation in silicate melts and their implications for the dynamics of explosive events, they do not directly link nanolite formation to processes of degassing, which is the major driving trigger of crystallisation in hydrous magmas ascending in volcanic conduits (e.g., Lipman et al. 1985; Cashman and Blundy 2000; Couch et al. 2003; Johnson et al. 2008; Applegarth et al. 2013; Allabar et al. 2020). Moreover, besides lunar basalts (e.g., Wieczorek et al. 2001), magmas erupted at superliquidus temperatures at the Earth's surface have not been documented. Only the recent work of Di Genova et al. (2020a) attempted degassing-driven experiments using a hydrous basalt that crystallised upon vesiculation. They monitored the formation of nanolites using synchrotron-based X-ray diffraction, small-angle X-ray scattering technique, and wide-angle X-ray scattering, but observed no in situ evidence of nanostructure formation.

To explore the link between degassing and crystallisation, we first analytically investigated post-degassing microstructures of synthetic dacitic samples from a previous study conducted by us (Pistone et al. 2017) and found that the nature of chemical heterogeneities of the residual silicate glass surrounding vesicles is suggestive of nanolites not observable at the microscale (1 µm). Then, we experimentally and analytically investigated the formation of nanolites induced by high-temperature degassing of dacitic melt, monitored in situ using scanning transmission electron microscopy (STEM) at high spatial resolution (0.4 nm). We observed the silicic melt undergoing decompression stimulated by thermal relaxation, followed by degassing and crystallisation at high temperature. Once microbubbles begin to form an interconnected porous network, dehydration of the melt triggers crystallisation of nanolites of quartz, plagioclase, clinopyroxene, and minor Fe-Ti oxides (at 1100 °C). We apply our experimental results to degassing processes in silicic melts of felsic magmas, and highlight that decoding the competition between initial bubble formation by degassing, favouring viscosity decrease and faster magma ascent, and release of gas via permeable pathways or outgassing and crystallisation, favouring viscosity increase and slower magma ascent, is key to understanding variations in eruption style at active volcanoes.

Experimental and analytical methods

Starting materials

Samples of previously hydrated and annealed mixtures of glass and quartz crystals were used in this study. Preparation of the starting materials is reported in detail in Pistone et al. (2016a); here we provide a short description of it. The felsic (F) composition is a synthetic approximation of the natural Adamello bulk composition JM101 (dacite/tonalite) reported by Blundy and Sparks (1992). Oxides (SiO_2, Al_2O_3, Na_2SiO_3) and hydroxides ($Al[OH]_3$, $K_2Si_3O_7{\cdot}3H_2O$) were used for material preparation, with hydroxides providing the amount of structurally bound H_2O to the felsic composition, with a total of 4.2 wt.% H_2O in the silicate glass. Aliquots of the dacitic glass were mixed with quartz particles (DORSILIT 2500 particles of 68 µm average size with aspect ratios between 1 and 3.5 from Alberto Luisoni AG, Switzerland) to produce starting materials of different crystal volume fractions as follows: F0 = 0.0, F50 = 0.5, F60 = 0.6, F70 = 0.7, and F80 = 0.8. Following the approach of Pistone et al. (2012), the starting material powders were cold-pressed into cylindrical stainless steel capsules (110 mm long, 35 mm inner diameter, 3 mm wall thickness) lined with a thin (25-µm) Mo foil. Filled capsules were stored at 100 °C to remove any adsorbed humidity, arc-welded shut,

hot isostatically pressed in an internally heated pressure vessel (Rock Physics and Mechanics Laboratory of ETH-Zurich) at 180 MPa and 1200 °C for 24 h, and finally cooled at 60 °C/min to ~ 100 °C above the glass transition temperature (~ 483 ± 3 °C based on calorimetric measurements using a Perkin-Elmer 8500 Differential Scanning Calorimeter at the University of Missouri, Columbia), followed by cooling at 0.6 °C/min to room temperature. During cooling the confining pressure decreased slightly with decreasing temperature by 3.8 MPa/minute and 0.1 MPa/minute in the first and second cooling stage, respectively (Pistone et al. 2016a). The final pressure of quenching of the starting materials was 68 MPa. After synthesis, cylindrical samples of 5.5 mm diameter and variable lengths (5.6 to 11.1 mm) were prepared. In addition, fine-grained (few µm diameter) powders of the crystal-free dacite glass were prepared using an agate mortar with ethanol. These powders were dried at 110 °C for 24 h prior to experimental investigation.

Degassing experiments

Here we consider the following two sets of degassing experiments: experiments from the work of Pistone et al. (2017) and experiments from this study using scanning transmission electron microscopy.

Pistone et al. (2017) conducted high-temperature (500 to 797 °C) experiments simulating degassing processes occurring in crystal-rich systems (crystal volume fraction, ϕ ranging from 0.5 to 0.8 on the gas-free basis). All the experiments were conducted using a Theta Industries Rheotronic III 1000C Parallel Plate Viscometer (University of Missouri, Columbia) at 0.1 MPa, with temperature monitored by a K-type thermocouple and a constant uniaxial stress of 0.63–0.64 MPa, produced by 1.5 kg load over cylindrical samples of 5.5 mm diameter. Room-pressure heating of hydrous samples quenched at high pressure (68 MPa) during synthesis allowed to simulate decompression-driven H_2O exsolution within reasonable conditions applicable to natural ascending silicic magmas, whose melt viscosity increases rapidly with H_2O removal (especially at < 1 wt.% H_2O; Hess and Dingwell 1996; Giordano et al. 2008; Romine and Whittington 2015), even during exceptional events of degassing induced by shear heating at the conduit margins (Lavallée et al. 2015).

The second set of new experiments from this study was conducted using a Hitachi Blaze heating stage, operating from room temperature to 1100 °C, inserted into a Hitachi SU-9000 low voltage scanning transmission electron microscope (STEM), hosted at the Georgia Electron Microscopy Center of The University of Georgia. Two different sets of experiments were conducted with the hot stage in the STEM. The first set were heating experiments, whereby images were collected during heating, with 100 °C increments between each step and a heating ramp rate between each temperature of 5 °C/s. Images were collected over the temperature range 500 to 1100 °C, with a total duration of 4 h and 30 min at high temperature conditions. The second set of experiments were isothermal and consisted of observing changes at a constant temperature of 900 °C over the course of 8 h. In this case, the sample was also heated from room temperature at a rate of 5 °C/s. All the experiments were conducted by monitoring degassing and crystallisation (i.e., formation of nanobubbles, microbubbles, and nanolites) in a time-resolved manner at different temperatures as follows: every ~ 20 min at 200–800 °C, ~ 10 min at 900–1000 °C, and ~ 5 min at 1100 °C. The temporal stepping of recording nanostructural changes induced by processes of degassing and crystallisation in situ is a function of the kinetics of these processes occurring at faster rate and shorter timescale with increasing temperature. We also recorded degassing processes including bubble coalescence every ~ 10 to ~ 20 s.

Micro- to nano-structural analyses

Backscattered (BSE) images of the tangential and central polished sections of the experimental charges from Pistone et al. (2017) were acquired on a field emission gun scanning electron microscope (SEM) FEI Nova NanoSEM600 (Smithsonian Institution) and a Hitachi S-3500 N SEM (University of Bristol) with 15 kV accelerating voltage and a beam current of 1 nA to obtain good contrast between glass, vesicles, and quartz grains.

Images of the samples undergoing in situ degassing using the STEM were simultaneously collected using the secondary electron, bright-field, and high-angle dark field detectors. Here we present secondary electron and bright-field observations. The bright-field observation was applied in the sample portions where the thickness of the glass (in very light grey colour) is small enough to visualise nanobubbles (in dark colour).

Chemical analyses of glass

Glass analyses in the peripheral and central sections of the run products from Pistone et al. (2017) were conducted across each sample domain along its length and width using 15 kV, 10 nA beam current, and beam scanning technique. The counting time on the peak and background positions for glass was: 30 and 15 s, respectively, for Si, Fe, Ca, Na, K, Mg, and Mn; 40 and 20 s, respectively, for Al, Ti, and P. Natural standards from the National Museum of Natural History (NMNH) of the Smithsonian Institution (Jarosewich 2002) were used and data were ZAF corrected using the Armstrong method oxide (Armstrong 1988): VG-2 (basaltic glass from Juan de Fuca Ridge [NMNH 111240-52]; Vogt and Byerly 1976; Byerly et al. 1977; Melson et al. 2002), VG-568

(rhyolitic glass from Yellowstone National Park [NMNH 72854-2]), and A-99 (basaltic glass from Makaopuhi Lava Lake, Hawaii, U.S. [NMNH 113498-1]; Wright et al. 1968; Wright and Fiske 1971; Wright and Okamura 1977; Byerly et al. 1977). Volatile content in the glass phase was estimated using the volatile by-difference method (Devine et al. 1995), with uncertainty of 1.04 wt.% based upon calibrating the analytical reproducibility at the chosen EPMA conditions with hydrous felsic glass of similar H_2O content (F0 from Pistone et al. 2016a, 2017; Table 1S), and by FTIR (see below). The volatile by-difference method accounted for the matrix corrections and element migration evaluated by analysing standard glasses during the analyses of the unknown glasses. However, our analysis does not account for the effect of sub-surface charging (Cazaux 1996; Hughes et al. 2019) that may cause element migration and changes in oxidation state during analysis (Hughes et al. 2018; Zhang et al. 2018). The volatile by-difference method is applied here to evaluate relative macroscopic changes induced by nano-phases (nanolites, nanobubbles) in the glass rather than determining the actual volatile content dissolved in the glass. Major element composition and related variances of the glasses of run products from Pistone et al. (2017) are reported in Table S1.

Target-oriented analyses of glass regions surrounding vesicles in the run product F50 were carried out using a CAMECA SX Five FE EPMA (University of Florida) using 10 kV, 20 nA, and 10-µm beam diameter. The counting time on the peak and background positions was 30 s and 15 s for Al, Ti, Ca, Mg, and P, and 10 s, and 5 s for Si, Fe, Na, and K, respectively. Mineral and glass standards were used and data were ZAF corrected as follows: albite, diopside, apatite, orthoclase, rutile, rhodonite, almandine, and HGG glasses (hydrous haplogranitic glasses with H_2O contents ranging from ~ 0 to 5.25 wt.%; Ardia et al. 2008). Volatile content in the glass phase was also estimated using the volatile by-difference method (Devine et al. 1995) described above. Here, the analysis was affected by minor Na loss (< 25%) due to the relatively large beam current (20 nA) at 10 kV (Morgan and London 1996) used to unravel small chemical changes (on the order of 0.5 wt.%) from glass to vesicle.

X-ray distribution maps of Si, Ti, Al, Fe, Mg, and Ca were acquired using the Oxford large area windowless energy dispersive spectroscopy (EDS) of the STEM at 30 kV and 10 µA.

We mapped the glass regions surrounding vesicles in the doubly polished run product F50 using Fourier Transform Infrared (FTIR) spectroscopy in transmission to quantify dissolved H_2O concentration in glass. FTIR was performed at the National Museum of Natural History of the Smithsonian Institution, with the Thermo Scientific Nicolet 6700 FT-IR Spectrometer coupled with a continuum IR microscope with motorised stage. We mapped the same glass area inspected by FE EPMA, which was optically crystal-and bubble-free across entire doubly polished wafer (sample thickness = 64 ± 2 µm). The sample was purged with dry, CO_2-free air during collection. We applied a 20 × 20 µm square aperture moving in 10 µm steps for high-resolution map (containing > 500 FTIR spectra). Each spectrum was collected over 600–6000 cm^{-1} wave numbers using 54 scans at 1 cm^{-1} resolution. Individual transmission spectra were reduced for estimating total H_2O at 3570 ± 1 cm^{-1} after fitting the spectral background with a spline function and calculating the net intensity of the absorbance band (Cottrell et al. 2018). The total H_2O concentration for the Fe-bearing dacitic glass (SiO_2 = 65 wt.% and FeO_{tot} = 3.8 wt.%; Pistone et al. 2016a) was calculated using the Beer-Lambert law using a thickness of 64 ± 2 µm, a glass density of 2400 kg/m^3, and the molar absorption coefficient ε_{3570} = 62.32 L/mol·cm for the total H_2O in evolved Fe-bearing (FeO_{tot} = 4.5–7.6 wt.%), hydrous (H_2O = 0.2–4.2 wt.%) andesite glass (SiO_2 = 57–65 wt.%) from Krakatau (Mandeville et al. 1996, 2002). As absolute thickness directly impacts absorption, the data near the vesicle walls (i.e., at distances < 10 µm from vesicle walls) are not reliable.

Results

Microstructures and glass chemistry of experimental run products of Pistone et al. (2017)

The 2D microstructural analysis of the experimental run products from Pistone et al. (2017) reveals complex microstructural domains characterised by different degrees of deformation, including ductile high-strain glass- and vesicle-bearing shear bands and brittle fractures across minerals, glass, and vesicles, and other sample domains dominated by clusters of vesicles surrounded by the pre-existing quartz grains (Fig. 1). Visual inspection at macroscopic scale of each run product suggests that the samples with high crystal contents ($\phi > 0.6$) display numerous through-going fractures, while samples with moderate crystal contents ($\phi = 0.5$–0.6) display numerous ductile shear bands. Moreover, sample crystallinity is inversely proportional to the vesicle content produced by degassing the same initial hydrous (4.2 wt.% H_2O) silicic melt. There are no appreciable differences in vesicle content between peripheral and central sections of each run product (within 0.02 bubble fraction, β). No evidence of cooling fractures (non-compliant with the field of deviatoric stresses applied during deformation) was found.

The collection of all chemical analyses of the residual glass phase in each run product reveals a monotonic decrease of Al_2O_3, MgO, FeO, and CaO with increasing SiO_2, while alkalis display modest variations, with Na_2O decreasing by ~ 10% relative and K_2O increasing by ~ 15% relative with increasing SiO_2 (Fig. 2). The glass of run product F80

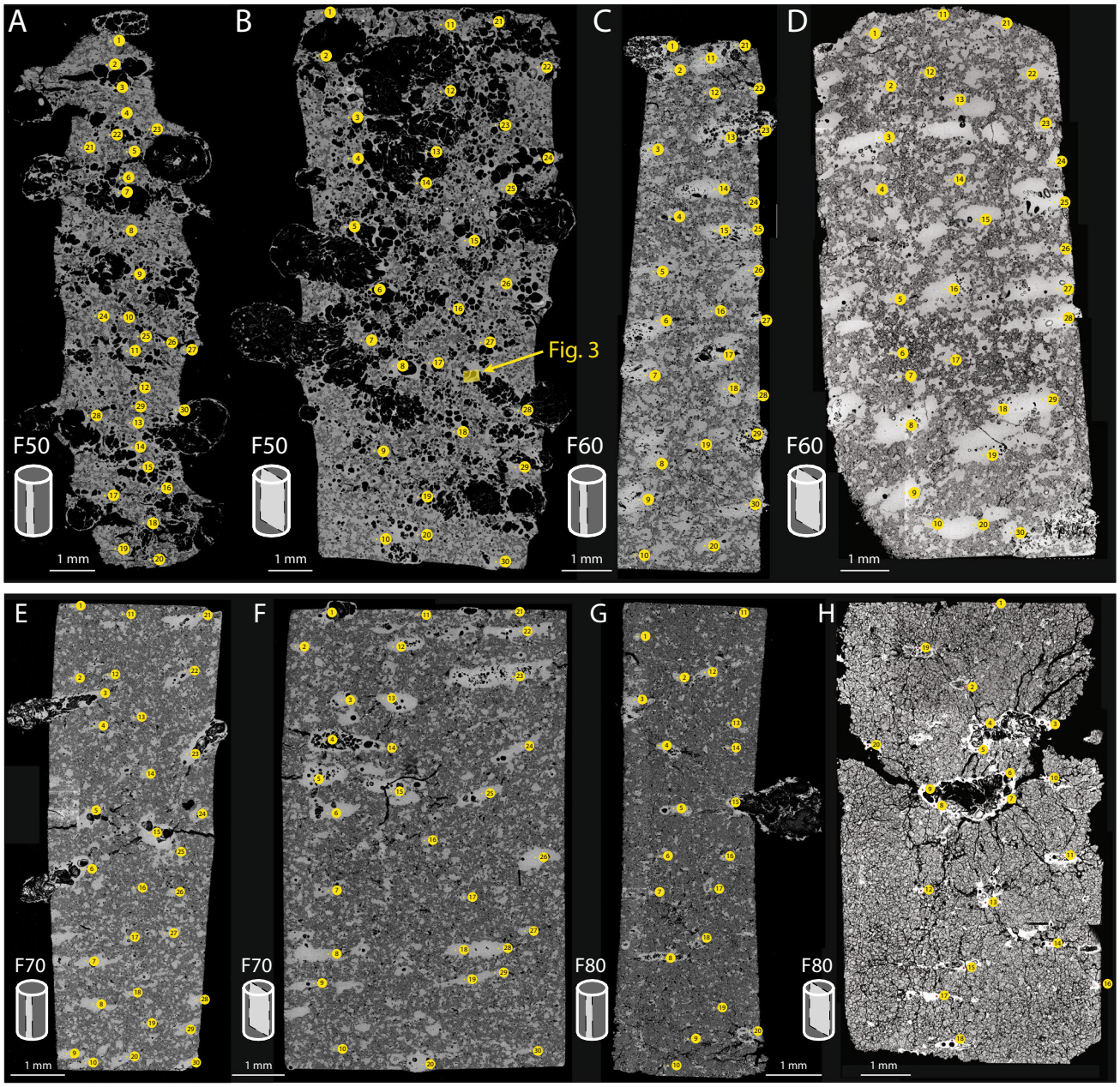

Fig. 1 SEM-based BSE images of tangential (**A**-**D**) and central sections (**E**–**H**) of the run products from Pistone et al. (2017), showing quartz crystals (dark grey), vesicles (black), silicate glass (grey), and fractures (black) in different volumetric proportions, arrangements, and interactions. Yellow dots accompanied by numbered yellow circles indicate locations of EPMA-based spot analyses and the corresponding number reported in Table S1. BSE images were acquired at the Smithsonian Institution (**A**-**C**, **E**–**G**) and University of Bristol (**D** and **H**). Panel B reports yellow area indicating the sample portion which the exploded view of Fig. 3 is from. Modified Fig. 4 from Pistone et al. (2017)

displays variable K_2O content, up to ~ 30% higher relative to the glasses in the other run products, at all SiO_2 contents (Fig. 2). TiO_2 decreases by up to 50% relative with increasing SiO_2; a few analysis spots indicate anomalously high concentrations of TiO_2 up to 1.2 wt.% in the residual glass (Fig. 2; Table S1). The volatile contents determined via the by-difference method appear to be very scattered. Most of the data tend to cluster at < 3 wt.% volatiles in the investigated SiO_2 range (Fig. 2). The volatile contents are poorly constrained in our analyses but they do suggest that the residual glass is chemically heterogeneous and not a single phase due to possible presence of invisibly small gas bubbles. The correlation between SiO_2 and the other major elements indicates a chemical shift driven by degassing

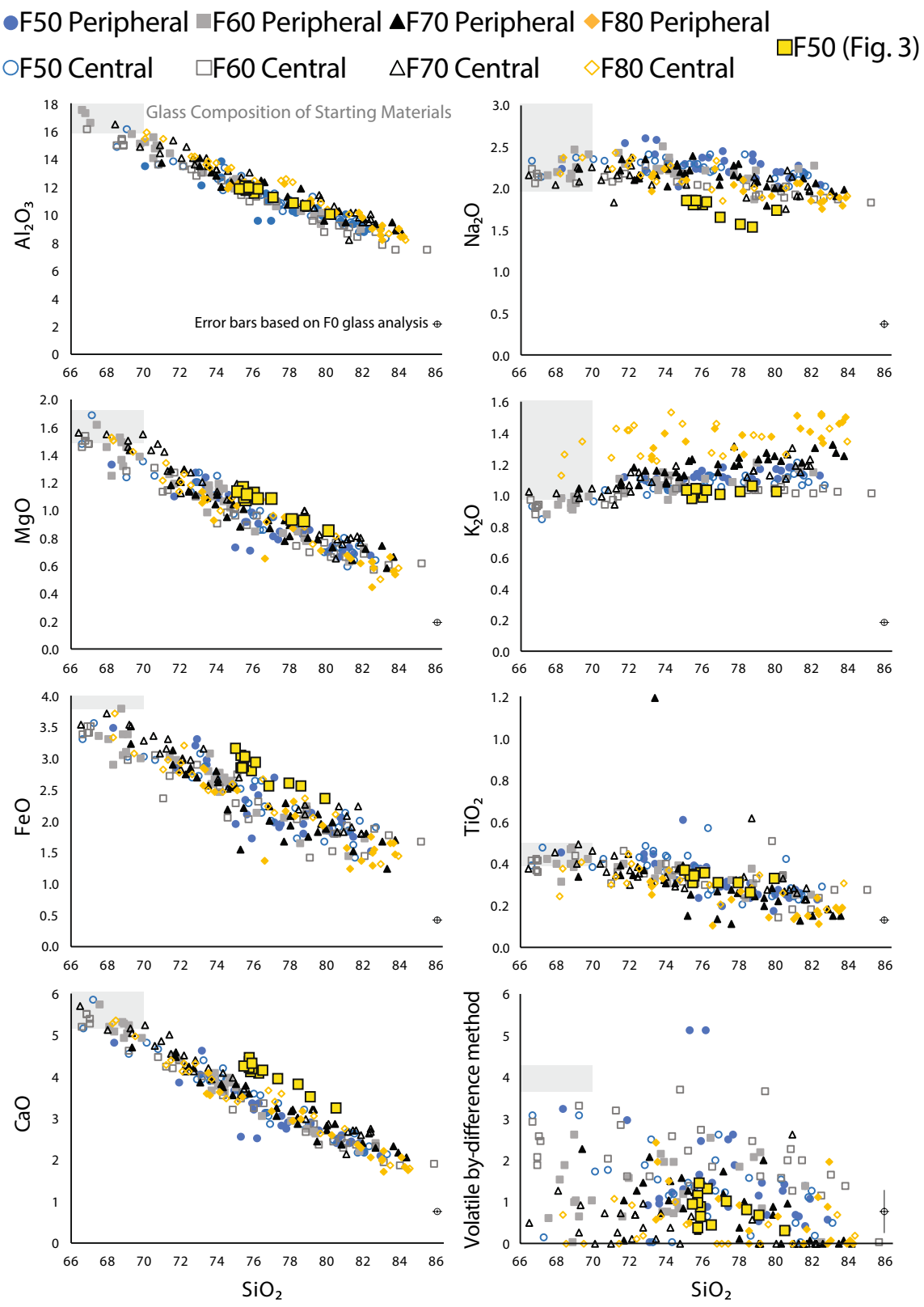

Fig. 2 Harker diagrams for major elements analysed by EPMA (on hydrous-basis). All coloured circles are data from conventional analytical conditions, whereas red squares are data acquired at higher spatial resolution and lower voltage. Details reported in text. Grey area indicates the compositional range of the starting glass of the run products from Pistone et al. (2017)

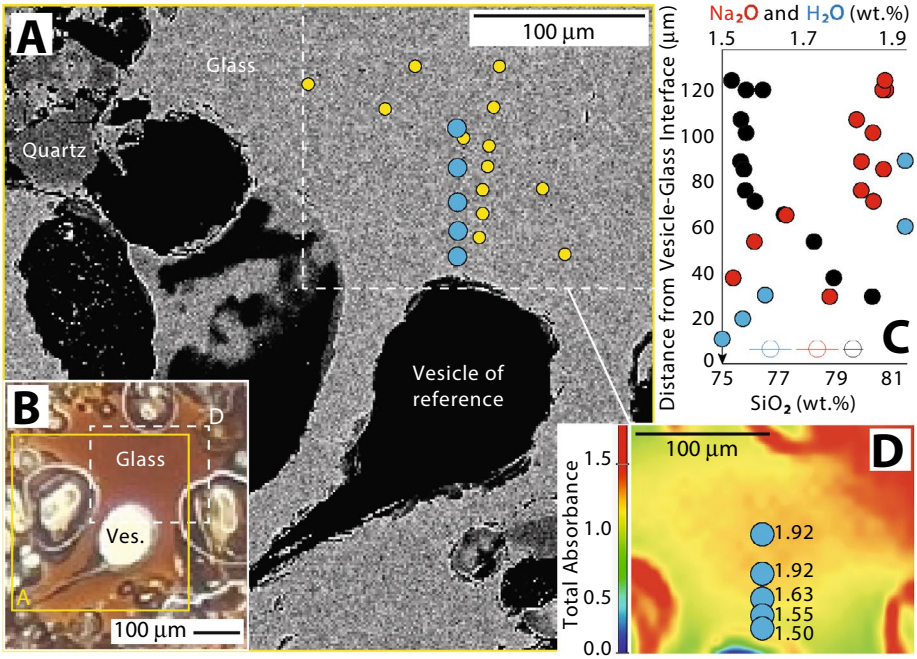

Fig. 3 **A** EPMA-based BSE image of detailed sample portion of the central section of run product F50 from Pistone et al. (2017). Dark phase is vesicle, dark grey phase is quartz, and light grey is glass. FE EPMA analysis spots are shown as yellow filled circles and FTIR grid points that were quantified for total H_2O (wt.%) are shown as blue filled circles. **B** Plane and transmitted light image of the sample (light brown is glass surrounded by whitish to dark vesicles). Solid yellow box shows area of the BSE image depicted in (**A**). Dashed white box shows area of FTIR map depicted in (**A**) and (**D**). **C** SiO_2 (black filled circles) Na_2O concentrations (red filled circles) (Table S1) and total dissolved H_2O (blue filled circles) in glass are reported as a function of the distance from the interface between glass and vesicle of reference depicted in (**A**). Error bars referred to data category (SiO_2, Na_2O, and H_2O) are reported as horizontal lines on coloured empty circles. **D** FTIR map of the sample area enclosed in the white dashed box of (**A**-**B**). The colour bar shows the total absorbance at 3750 cm^{-1}

and crystallisation processes, but without evidence of even incipient crystallisation of the glass matrix at the microscale though. The increase of SiO_2 and concomitant change of the other major element concentrations as described above tend to be localised in regions populated by numerous vesicles (Fig. 1). Target-oriented chemical transects of analysis spots from glass to vesicle in F50 (Fig. 3A, B) confirm a similar trend observed at the scale of the whole run product. In F50, the closer to the vesicle, the more evident the compositional change of the residual glass, which increases in SiO_2 (Fig. 3C) and decreases in Al_2O_3, MgO, FeO, and CaO (Fig. 2). Along this analysis spot profile, TiO_2 and K_2O concentrations in the glass remain fairly constant (Fig. 2), whereas H_2O contents measured by FTIR and Na_2O contents measured by FE EPMA decrease as the vesicle is approached (Fig. 3C). We note that absolute Na_2O concentrations are affected by partial Na_2O loss (up to 0.4 wt.% absolute or ~ 20% relative) due to the application of relatively high current (20 nA) during FE EPMA analysis, with small offsets between FeO, CaO and, to a more limited extent, MgO from the general trend (Fig. 2). Loss of Na under the electron beam cannot explain the strong systematic decrease in Na_2O of ~ 1.4 wt.% as the vesicle is approached (Fig. 3C). The H_2O content in the residual glass decreases by 22% from 1.92 wt.% in the central portion of the glass region to 1.5 wt.% at ~ 10 µm from the vesicle (Fig. 3C, D).

Nanostructures and glass chemistry of experimental run products from in situ secondary electron and bright field observations

The secondary electron and bright field observations collected during the heating experiments by STEM (Fig. 4) reveal no tangible nanostructural changes in the melt of sample F0 starting from 500 to 800 °C (Fig. 4A). Changes at nanoscale start from 900 °C and involve formation of dark coloured open (i.e., connected to the sample surface) subspherical nanovesicles of ~ 20 to 80 nm (Fig. 4B). In the temperature range between 900 and 1000 °C, during gas exsolution, the formation of new light grey phases in the melt occurs under secondary electron observation. Such phases are not clearly connected to the surrounding visible vesicles (Fig. 4B). At 1100 °C, the light grey phases grow more remarkably in the melt and either appear to be

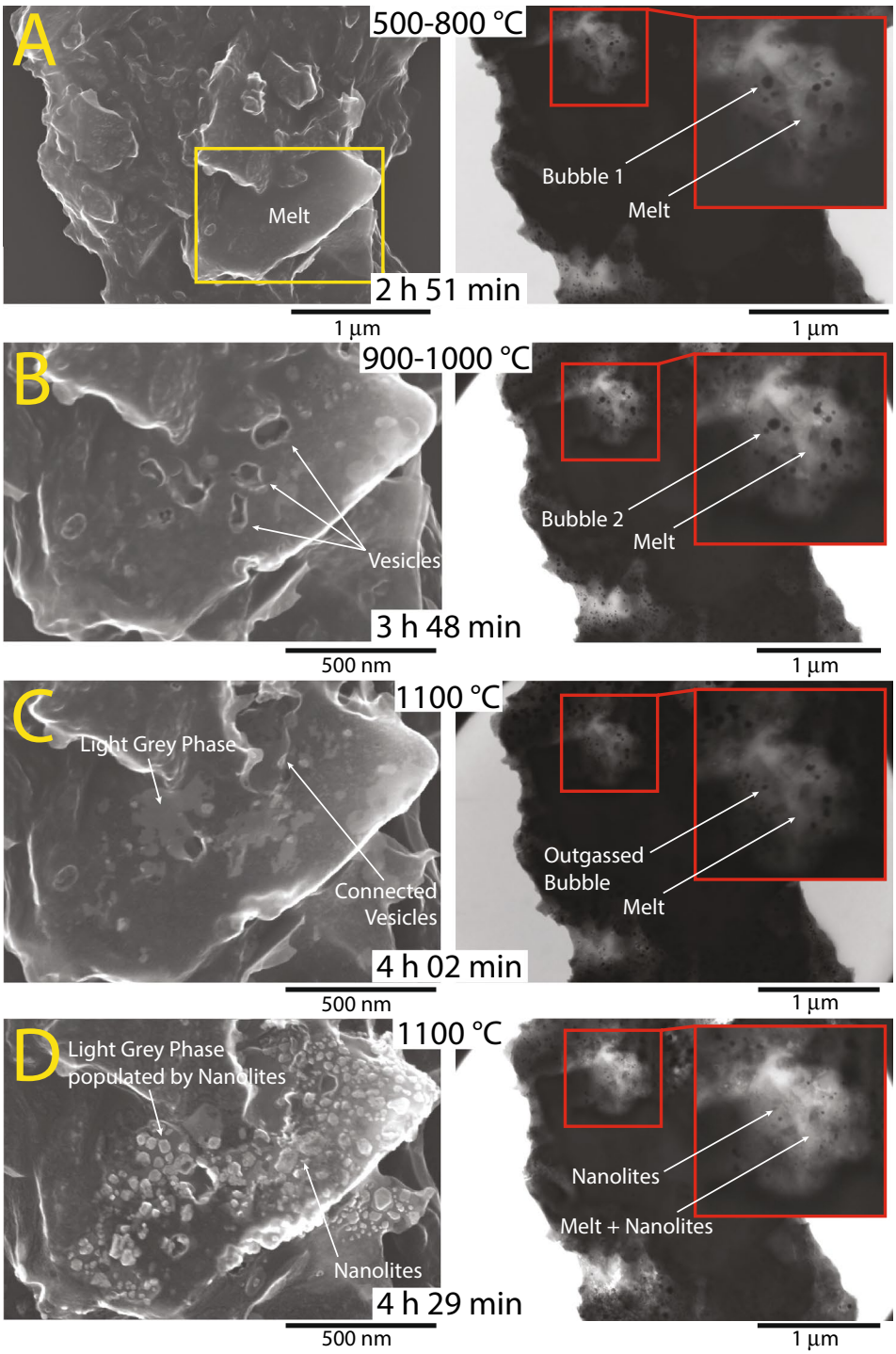

Fig. 4 STEM-based time-elapsed view of development of nanoporosity and nanolites in sample F0 in secondary electron (left column) and bright field observations (right column) collected during heating experiments. Grey phases are plagioclase and clinopyroxene, bright roundish phases are oxides, dark open phases are vesicles, dark grey areas are quartz grains in very dark grey melt, bright areas are sample edges characterised by charge effect, very light grey areas are unidentified phases in this experiment

connected to the residual vesicles or occupy the melt regions where other vesicles were located prior to outgas (Fig. 4C). In the bright field, the decrease of number of observable vesicles in the melt is augmented up to 50% (Fig. 4B, C). After 27 min under the same temperature, the melt appears to be largely populated by several solid mineral phases that are in direct contact with the residual large bubbles (up to 100 nm), which adapt their shape within the available residual melt and form nanominerals (Fig. 4D). At the full scale of observation, sample F0 displays a strongly "crispy" texture formed by mobile bubble surfaces at the highest temperature of the experiment (Fig. 4D).

A combination of high-resolution observation and EDS-based chemical analysis of major elements allows to identify the different nanominerals produced in the residual melt during degassing at 1100 °C (Fig. 5). Specifically, we identify

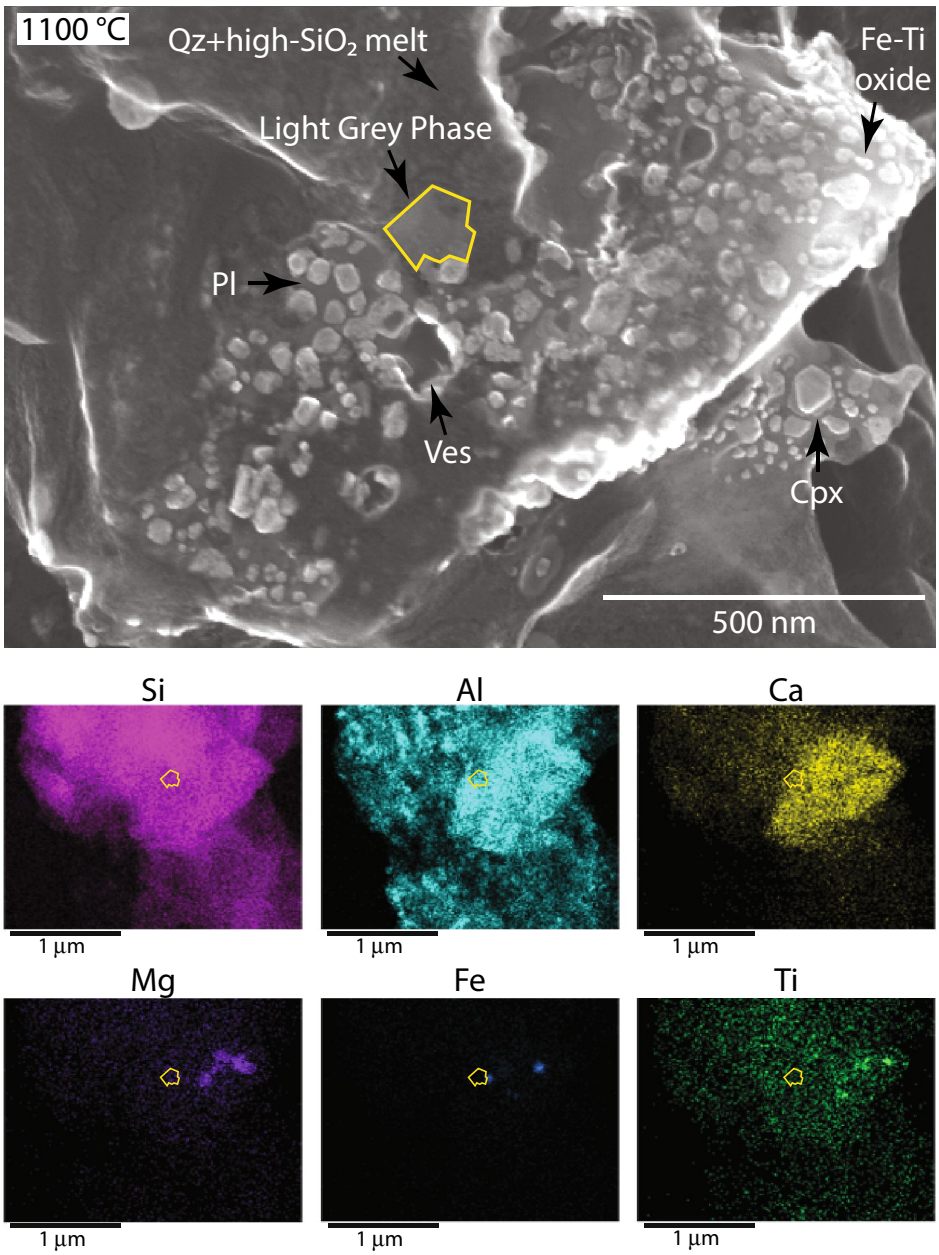

Fig. 5 Secondary electron view of the final temperature step of the STEM-based heating experiment showing both nanoporosity and nanolites, with exemplary light grey phase indicated by yellow polygon in sample F0. EDS-based X-ray distribution maps of major elements of the selected sample area. Grey phases are plagioclase and clinopyroxene, bright roundish phases are oxides, dark open phases are vesicles, dark grey areas are quartz grains in very dark grey melt. Bright areas are sample edges characterised by charge effect. *Ves* vesicle, *Pl* plagioclase, *Cpx* clinopyroxene, *Qz* quartz

the presence of subspherical Fe-Ti oxides (up 10 nm size), tabular plagioclase (up to 40 nm size), clinopyroxene (up 50 nm size), and quartz (up to 30 nm size), all embedded in high-SiO_2 silicate melt (Fig. 5). While plagioclase, clinopyroxene, and Fe-Ti oxides form crystal clusters altogether, quartz is mainly found in regions populated by dark-coloured melt. Quartz and melt are the most difficult for phase discrimination due to the very low density contrast in secondary electron observation. The light grey phase identified starting from 900 °C (Fig. 4) appears to be enriched in Si, Al, and Ca and connected to nanominerals of plagioclase, clinopyroxene, and Fe-Ti oxides and bordered by some vesicles (Fig. 5). From a compositional standpoint, this phase may indicate presence of plagioclase, but the nanostructure is not equivalent to a properly formed mineral.

The secondary electron imaging applied during the isothermal experiments by STEM at 900 °C captured the dynamics of bubble formation, impingement, and connectivity during silicate melt degassing of sample F0 (Figs. 6 and 7). Here, we observe the cohabitation of gas pockets enveloped in silicate melt (gas bubbles) and open, outgassed vesicles, with the latter growing during time. The bubble impingement produces a pattern of hexagonal shaped features similar to a honeycomb structure as a result of the maximum packing fraction of bubbles forming a gas foam (Fig. 6A). We observe the in situ degassing followed by

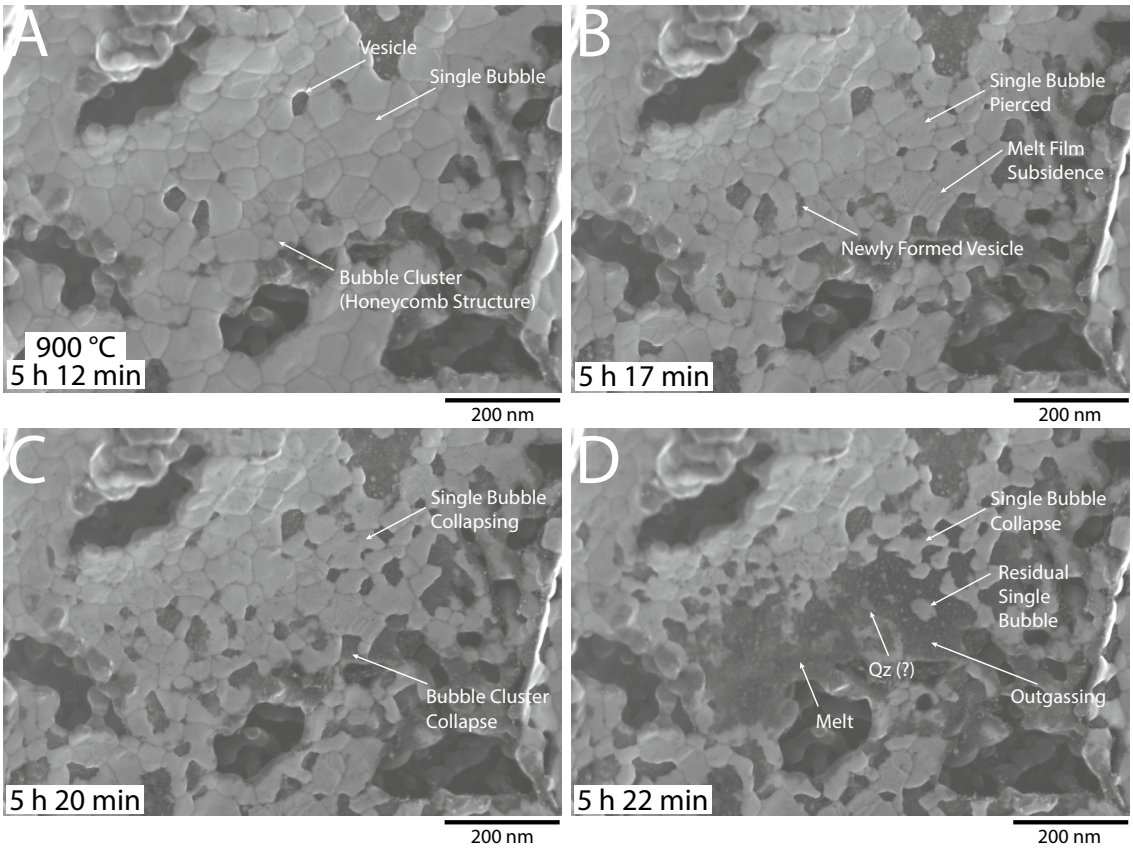

Fig. 6 **A**–**D** STEM-based time-elapsed secondary electron view of development of nanobubbles (light grey phases) that grow, impinge (**A**), and connect forming vesicles (dark areas) (**B**) after connected bubble collapse (**C**–**D**) during isothermal experiments conducted on sample F0. Time is reported as cumulative time since the beginning of the experiment. Bright areas are sample edges characterised by charge effect. *Qz* quartz

outgassing through permeable gas pathways represented by vesicles. Once bubbles connect, the melt film surrounding them start to destabilise by getting pierced and fractured (Fig. 6B), followed by a general bubble surface subsidence (Fig. 6C) that produces a cascade effect leading to bubble collapse and outgassing (Fig. 6D). At finer scale, gas release is identified by holes that pierce either the edges of neighboring bubbles or within the bubble central portion (Fig. 7A). The holes formed at the bubble edges continuously grow at the expense of the previous bubbles and follow the edges/margins of the other surviving bubbles, forming open vesicles (Fig. 7A). Gas connectivity rapidly evolves into regions of topographic depression, which are large open vesicles of several hundreds of nm size (Fig. 7B-D). Such vesicles showcase open tubes into the sample domain with "crispy" margins/surfaces of unconnected bubbles and small holes/tubes connected to the main one (Fig. 7B-D). Bubble collapse due to gas connectivity is evidenced by wrinkles in the silicate melt enveloping the gas bubble, which progressively gets pierced by multiple holes (of 10 nm size) and linear fractures along the bubble perimeter. Holes and fractures lead to the structural subsidence and collapse of the bubble surface due to gas escaping through the connected permeable network (Fig. 7F). Bubble collapse and disappearance is either followed by the formation of an open vesicle (Fig. 7B-D) or by silicate melt with suspended phases that may resemble quartz grains (Fig. 7G, H). In our time-elapsed observation, the overall process of bubble coalescence and release accompanied by silicate melt films rupturing occurs within few tens of seconds at nanoscale (Fig. 7E-H), whereas the development of micro-sized vesicles occurs in < 10 min (Fig. 7A-D).

Discussion

Degassing-induced nanoporosity and bubble coalescence by melt film resonance

The experiments performed at nanoscale using the STEM shed light on the causes leading to the chemical heterogeneities around vesicles observed in the experimental

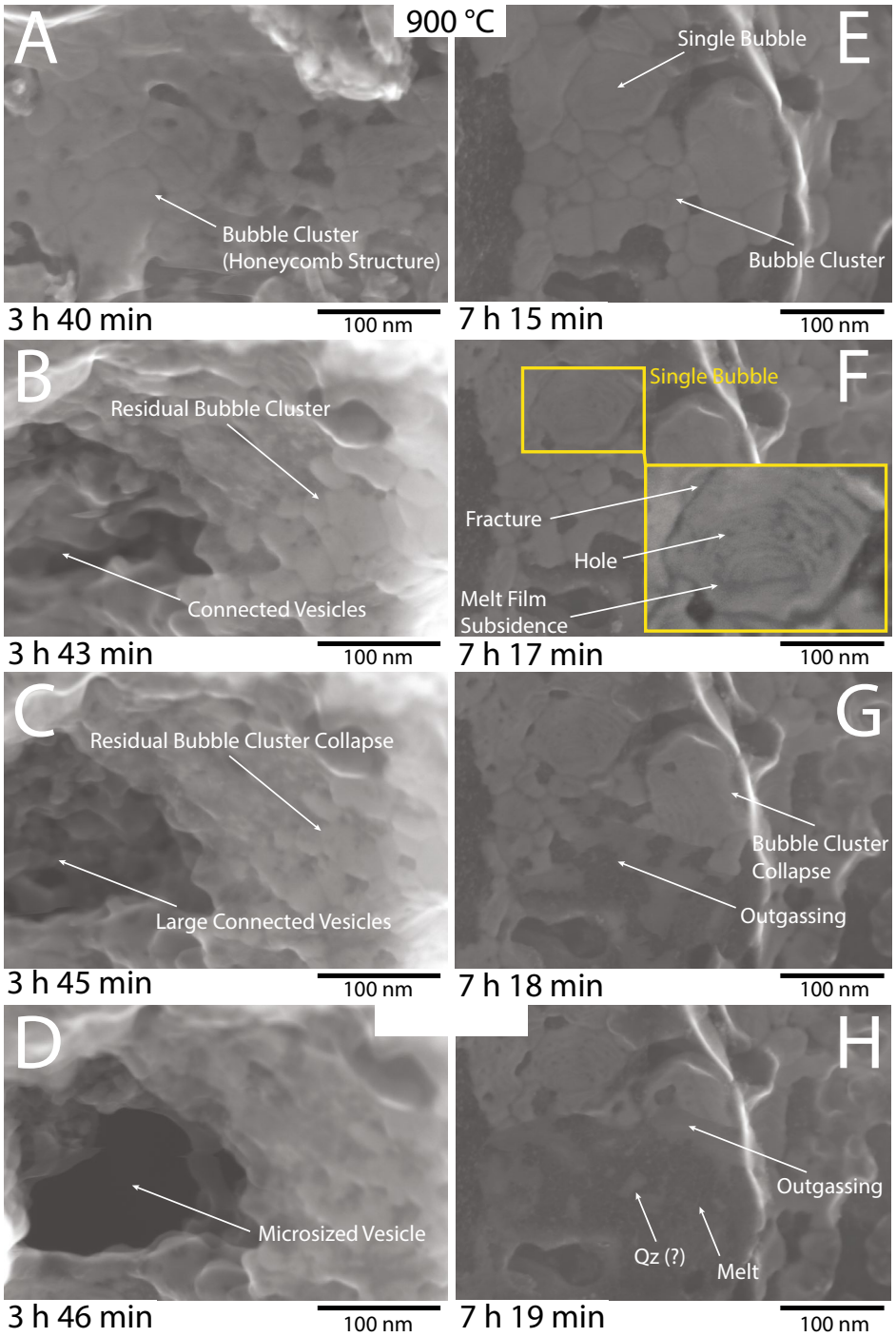

Fig. 7 **A**–**D** STEM-based time-elapsed secondary electron view of development of nanobubbles (light grey phases) that grow, impinge, and connect forming vesicles (dark areas) at microscale during isothermal experiments conducted on sample F0. **E**–**H** Detailed observation of bubble impingement (**E**), subsidence through gas connectivity (**F**) and subsequent bubble collapse by outgassing (**G**) followed by formation of incipient quartz in the residual silicic melt (**H**). Time is reported as cumulative time since the beginning of the experiment. Bright areas are sample edges characterised by charge effect. Yellow inset shows bubble-melt interface wrinkles accompanied by holes and linear fractures during bubble collapse. *Qz* quartz

run products from the work of Pistone et al. (2017). The observed depletion of Al_2O_3, MgO, FeO, CaO, and, to a lesser extent, TiO_2 (Fig. 2) can be explained by the generation of clusters of nanobubbles (filled with H_2O) and open vesicles (outgassed voids) within an illusory homogeneous glass shell around the vesicles when observed at microscale (Fig. 3). The generation of nanoporosity (bubbles + vesicles), accompanied by incipient crystallisation of quartz (Figs. 6D, 7H), locally shifts the initial glass/melt composition to high SiO_2 contents, with relatively constant alkali concentrations (Fig. 2). At large scale of observation (hundreds of microns), we may speculate that the homogeneity of alkali concentrations across the investigated glass may be related to the relatively large diffusivity of alkali as network-modifying species through the silicate melt (~ 10^{-11} m^2/s at 700–800 °C in a silicate melt bearing 3.5 wt.% H_2O;

van der Laan and Wyllie, 1993). However, at more local spatial scale (on the order of 60 µm) around the bubble, variations of alkali concentrations in glass are clearly found (Fig. 3), testifying chemical heterogeneities are not exclusively driven by diffusion processes, but also by H_2O exsolution and crystallisation.

If the presence of nanoporosity is as dominant as observed in the STEM experiments at 900 °C (Figs. 6 and 7), we may interpret that the large scattering of volatile contents (Fig. 2) could be caused by the presence of both H_2O-rich nanobubbles and vesicles devoid of H_2O, heterogeneously arranged at the microscale during degassing processes (Figs. 4, 5, 6, 7), and ultimately coalescing and leading to the generation of large vesicles (Figs. 1, 3, 7A-D). In this context, the variation of residual H_2O content on the scale of tens of microns (Fig. 3C, D) could be related to diffusion of H_2O out of the melt and into bubbles as recorded by natural samples (Castro et al. 2005, 2012; Cabrera et al. 2010; Schipper et al. 2013). This contrasts with hydration processes leading to spherulite formation (Castro et al. 2008; Watkins et al. 2009; Gardner et al. 2016) or resorption of bubbles upon cooling (McIntosh et al. 2014), both of which will lead to H_2O concentration increase in the glass. The combination of microscale major element and H_2O analyses of the glass in the run products from Pistone et al. (2017) do not clearly reveal the presence of nanolites, as these phases appear to form at temperatures exceeding 900 °C at the nanoscale resolution applied in our study (Figs. 4 and 5). At such high temperatures, the same starting dacitic to rhyolitic hydrous melt is forced to degas more vigorously with formation of numerous nanobubbles, which rapidly impinge against each other, coalesce, and produce open permeable vesicles that outgas H_2O and dehydrate the overall sample (Fig. 6).

At the spatial scale of our time-resolved observations, the formation of bubbles appears to occur without assistance of crystal substrates or other phases in the crystal-free sample F0, and results from the large supersaturation pressure of the starting melt (originally quenched at 68 MPa). It is known that heterogeneous bubble nucleation tends to be dominant in multiphase magmatic systems undergoing degassing upon ascent (Shea 2017; Hajimirza et al. 2021). Intrinsic heterogeneities such as amorphous phase separation, chemical melt demixing, and incipient crystallisation of nanolites (Binder 2015; Mujin et al. 2017; Di Genova et al. 2020a) can play a key role in promoting the nucleation of gas bubbles in partially molten materials (Höche et al. 2011; Cormier 2014; Deubener et al. 2018; Kleebusch et al. 2018; Zandona et al. 2019; Di Genova et al. 2020b). To the best of our time-resolved observations during the whole duration of each STEM experiment, we only observe first the nucleation of nanobubbles in the silicate melt followed by nanocrystals generated during gas release by connectivity between nanobubbles (Figs. 3,4,5 and 6). The possible absence of unidentified nanocrystals is corroborated by the relatively homogenous distribution of nanobubbles produced in the silicate melt at nanoscale (up to 1000 nm; Figs. 6A, 7A).

The polygonal network of impinged bubbles forming borders made of thin melt films separating the gas pockets (Bikerman 1973; Kraynik 1988) is then disrupted by bubble coalescence in a cascade effect. Bubble coalescence occurs by melt film instability evidenced by wrinkles on the melt/bubble interface, later pierced by holes and peripheral fractures that indicate melt film rupture between adjacent bubbles (Figs. 6C, D and 7F). This mechanism is quite different from vesiculation through melt film thinning by stretching between expanding gas bubbles as described in previous works examining gas connectivity at microscale (Proussevitch et al. 1993; Martula et al. 2000; Okumura et al. 2006; Gardner 2007; Castro et al. 2012; Nguyen et al. 2013; Martel and Iacono-Marziano 2015; Giachetti et al. 2019).

We infer a sort of resonance of wavy vibrations on the melt film surrounding the bubble due to gas migration through permeable pathways that lead to melt-bubble interface subsidence and collapse (Figs. 6B-D and 7E-H). In the light of the time-resolved observations, such vibrations increase in frequency until the melt is no longer relaxed that fails in a brittle manner (Fig. 7E, F). Unfortunately, the time-elapsed acquisition of the STEM-based observations at nanoscale does not capture continuously the shift of the melt film disturbance from low to high frequency. This resonance of the viscoelastic melt is a known phenomenon in acoustic properties of bubbly magmas (Ichihara and Kameda 2004; Kurzon et al. 2011; Tisato et al. 2015; Karlstrom and Dunham 2016; Melnik et al. 2020). In this case, the melt vibration is triggered by the gas movement through H_2O diffusion from melt into bubble and exsolved H_2O migrating along permeable pathways (holes and linear fractures) that, in turn, destabilise neighbouring bubbles that collapse and destroy the original polygonal network in an irreversible cascade effect (Figs. 6 and 7).

Bubble coalescence in initially crystal-free felsic melt occurs at a critical gas volume or "percolation threshold" (Stauffer and Aharony 1994; Blower 2001; Blower et al. 2001; Walsh and Saar 2008) values ($\beta > 0.9$; Figs. 6 and 7) that are more consistent with permeable reticulite pumices than largely impermeable crystal-free and crystal-poor systems analysed at microscale ($\beta < 0.78$; Eichelberger et al. 1986; Sahimi 1994; Garboczi et al. 1995; Klug and Cashman 1996; Saar and Manga 1999, 2002; ″ et al. 2003; Takeuchi et al. 2005; Burgisser and Gardner 2005; Mueller et al. 2005, 2008, 2011; Namiki and Manga 2008; Polacci et al. 2008; Wright et al. 2009; Rust and Cashman 2004; 2011; Nguyen et al. 2014; Farquharson et al. 2015; Lindoo et al. 2016; Wadsworth et al. 2016; Burgisser et al. 2017; Colombier

et al. 2017; Gonnermann et al. 2017; Kushnir et al. 2017; Vasseur and Wadsworth 2017; Vasseur et al. 2020). The unconnected/impermeable porosity of 0.9 was achieved in heating experiments at ~ 1024 °C in initially H_2O-poor (0.24 wt.%) rhyolitic obsidians (Pistone et al. 2015a). At microscale, such high porosity was interpreted as the result of a combination of three factors: the presence of pre-existing vesicles in the starting glass prior to heating, rapid heating rates (30 °C/s), and short experimental duration (< 14 s; Pistone et al. 2015a). In this study, we show that gas impingement and maintenance of high porosity prior to coalescence and then release via permeable pathways can persist for long durations (several hours) even at high temperatures (≥ 900 °C). High temperature favours lower melt viscosity and faster melt relaxation (Hess and Dingwell 1996), until H_2O loss from the melt by degassing becomes the dominant factor that, conversely, favours the increase of melt viscosity and susceptibility to rupture (Dingwell and Webb 1989; Hess and Dingwell 1996).

Degassing-induced liquidus temperature rise and melt nanocrystallisation

Melt dehydration by H_2O degassing moves the H_2O-saturated solidus for near-eutectic felsic systems to higher temperature (Tuttle and Bowen 1958; Cann 1970; Harris et al. 1970; Johannes and Holtz 1996; Balashov et al. 2000; Blundy et al. 2006; Glazner 2019). During our high-temperature experiments, the system continuously degasses H_2O (originally dissolved in the silicate melt quenched at 68 MPa during synthesis) from melt into bubbles in a fashion similar to decompression heating (McKenzie and Bickle 1988; Glazner 2019). During decompression heating an initially high-pressure system slides along the H_2O-saturated solidus to conditions of lower pressure and higher temperature, induced by H_2O loss from the melt by degassing. In our experiments, the sample is heated and progressively dehydrates, simulating the system degassing upon decompression. Under these conditions, for which residual H_2O contents are expected to be well below 1 wt.% at > 800 °C (Pistone et al. 2015b), the liquidus temperature rises and stimulates the nucleation and growth of nanolites upon bubbles/vesicles still trapped in the melt or in the melt regions previously populated by bubbles/vesicles (Figs. 4 and 5).

From a petrological standpoint, we observe the simultaneous formation of mineral phases such as plagioclase, clinopyroxene, Fe-Ti oxides (ilmenite and magnetite), and quartz, consistent with H_2O-saturated (≤ 4.2 wt.%), low-pressure (≤ 68 MPa, as a function of H_2O degassing from the residual rhyolitic melt), high-temperature (800 to 1100 °C), and relatively oxidising (NNO + 1 to + 2) andesitic to rhyolitic systems (Blatter and Carmichael 1998, 2001; Moore and Carmichael 1998; Blatter et al. 2001). The newly formed minerals (mainly plagioclase) are arranged in dense clusters pervaded by residual melt films of < 1 nm thick (Fig. 5). Following the seminal studies of Cahn (1961), Binder and Stauffer (1974), and Cormier (2014), formation of single nanocrystals and clusters of nanolites can be modulated by a combination of spinodal decomposition induced by chemical heterogeneities and *sensu stricto* nucleation leading to the separation of the solid phase from the original silicate melt (Binder 2015). The observed formation of nanocrystals in our experiments can be related to the generation of chemical heterogeneities of the melt (i.e., increase of the silica content) induced by the formation of nanobubbles. Indeed, recent preliminary analyses using electron energy-loss spectroscopy and atom probe tomography revealed that chemical heterogeneities in the vicinity of gas bubbles start to occur at sub-nanometer scale and highlight an equivocal scenario in which mineral nuclei *or* gas bubbles may form first during hydrous melt degassing and crystallization (Dubosq et al. 2021). These nanolite clusters formed in nearly eutectic-based melt composition, that, before the evident appearance of nanolites, evolves from a dacite (66–74 wt.%) to a "normal" rhyolite (74–78 wt.%) and a "ultra-high silica rhyolite" melt (78–84 wt.%) at ~ 3 wt.% total alkali (Fig. 2) using the total alkali versus silica plot (Le Maitre et al. 2002). The observed silica increase of the residual melt is a function of the increase of porosity (bubbles + vesicles composing the light grey phase identified during the heating experiments, Fig. 4C) and possible presence of quartz (Figs. 6D and 7H) at nanoscale. Especially, these chemical changes in the residual glass inspected analytically at microscale occur in proximity of vesicles that become permeable routes of H_2O loss from the sample (Figs. 4, 5, 6 and 7). Gas exsolution driving undercooling is an important process that stimulates mineral formation (Hammer and Rutherford 2002; Couch et al. 2003; Martel and Schmidt 2003; Brugger and Hammer 2010; Cichy et al. 2011; Martel 2012; Mollard et al. 2012; Arzilli and Carroll 2013; Riker et al. 2015a; b; Waters et al. 2015; Befus and Andrews 2018). Then, the chemical heterogeneities observed at the vesicle-glass interface in our run products at microscale (Fig. 3C) may be related to physical and chemical changes induced by the generation of nanolites of quartz following the formation of nanoporosity (Figs. 6 and 7) rather than chemical diffusion-driven processes. At < 900 °C, diffusivities of major elements are very low ($< 10^{-11}$ m^2/s; van der Laan and Wyllie 1993) and, consequently diffusion length scales are expected to be on the orders of few microns, which cannot explain chemical variations in the order of 60 µm length scale (Fig. 3C). A possible physical process that may lead to such chemical heterogeneities is a combination of melt expulsion during nanoporosity formation (similar to gas-driven filter pressing; Pistone et al. 2015b) and incipient formation of quartz nanolites (Figs. 6D and 7H). Once the H_2O is released and

the melt becomes highly H_2O-poor and near-solidus, nanolites form and can be clearly observed using STEM (Figs. 4, 5, 6 and 7).

Degassing at low H_2O concentrations in the melt (< 0.5 wt.%; Applegarth et al. 2013) can lead to rapid crystallisation (Hoblitt and Harmon 1993; Wright et al. 2007) up to $\phi \sim 0.3$ in mafic systems (Applegarth et al. 2013). In our experiments simulating degassing of viscous silicic melt, ϕ reached up to ~ 0.5 in the sample regions explored at nanoscale, but only after degassing for several hours at 900 °C, tens of minutes at 1000 °C, or a few minutes at 1100 °C (Fig. 4). The kinetics of crystallisation in felsic melts is known to be generally slow at < 800 °C (e.g., Bagdassarov et al. 1996; Befus 2016), but, with degassing induced by heating, crystal nucleation and growth can be considerably accelerated (e.g., Cashman and Blundy 2000; Waters et al. 2015), as observed in our experiments starting from 900 °C with incipient crystallisation of quartz (Figs. 6D and 7H) and enhanced crystallisation of quartz, plagioclase, clinopyroxene, and Fe-Ti oxides at 1000 and 1100 °C (Fig. 4C, D). As the experiments were run either with stepwise heating or isothermally, we did not explore the influence of effective decompression rate due to heating-induced H_2O exsolution on the generation of nanolites.

Previous observations of gas exsolution at 1100 °C stimulated by high heating rates and very short timescales indicated that the radius of gas bubbles grew at ~ 1 µm/s and no microlite formation was observed (Pistone et al. 2015a). Although these samples were not inspected on the nanoscale, nanolite formation is expected to be very improbable due to the short duration of the simulated vesiculation of silica-rich melts (< 14 s; Pistone et al. 2015a). Previous studies reporting synthesis of hydrous phonolite, dacite, and rhyolite glasses in internally heated pressure vessels (Schiavi et al. 2018; Allabard et al. 2020; Giordano et al. 2021; González-García et al. 2021) have shown the formation of nanolites with cooling rates ranging from 200 °C/min to 16 °C/s within 3 min to 50 s of cooling from high-temperature conditions (1000–1250 °C) to the glass transition temperature. The timescales of the internally-heated pressure vessel experiments are longer than the timescale of vesiculation measured by Pistone et al. (2015a). However, lower H_2O content and larger undercooling might favour the formation of nanolites on short timescales (on the order of milliseconds), as observed during the synthesis of anhydrous glasses ranging from basalt to rhyolite (Di Genova et al. 2017a, b; 2020a, b; Kleest et al. 2020).

In the present study, nanolite formation occurs once initially retained nanobubbles largely outgas from the sample (Fig. 5). Therefore, the nucleation and growth of nanolites is favoured when melt degassing is sustained for reasonable duration at specific temperature (hours at 900 °C, tens of minutes at 1000 °C, and several minutes at 1100 °C) and once gas bubbles are readily removed from the sample, leaving behind a relatively anhydrous, near-solidus residual melt. Such a mineral formation mechanism is consistent with previous findings on crystallisation kinetics in magmas that demonstrate that high heating rates or decompression rates (generating large undercooling) suppress crystallisation in felsic systems (Hammer and Rutherford 2002; Couch et al. 2003; Martel and Schmidt 2003; Brugger and Hammer 2010; Cichy et al. 2011; Martel 2012; Mollard et al. 2012; Arzilli and Carroll 2013; Riker et al. 2015a; b; Waters et al. 2015; Befus and Andrews 2018).

Degassing-induced magma mobility with nanoporosity and magma stalling with nanocrystallisation: implications on magma ascent and fragmentation in volcanic conduits

The STEM-based experiments show that, at nanoscale, degassing processes in silica-rich systems generate: first, a foam of clustered gas bubbles that largely populate the hydrous melt; second, once the gas bubbles connect and outgas, nanolites form and increase the crystal content of the residual melt. These two stages of the degassing-induced crystallisation process are expected to exert a crucial influence on the rheological behaviour of the silicate melt and, by inference, on the transport of magma in volcanic conduits.

At 900 °C, the silicic melt is so enriched in nanobubbles that the viscosity of the bubble-bearing suspension may increase if bubbles behave similarly to solid particles ($Ca > 1$; Llewellin et al. 2002) or may decrease in the presence of deformable bubbles ($Ca < 1$; Llewellin et al. 2002). Within a crystal-rich magma ($\phi > 0.3$; i.e., crystal mushes; Marsh 1981; Bachmann and Bergantz 2004) carrying microlites and/or phenocrysts, such bubble-bearing melts are gas foams with low density and high buoyancy (Gonnermann 2017) and, under intensive deformation, substantially favour the flow of magmas. The rheological experiments at ~ 700 to ~ 800 °C conducted by Pistone et al. (2017) (Fig. 1) simulated the extrusion of crystal-rich lava domes experiencing large decreases of bulk viscosity, controlled by crystals, bubbles, and silicate melt arranged in different modal proportions. Based on chemical inspection along a glass-vesicle transect (Fig. 3C), the areas populated by the "invisible" nanobubbles that cause chemical changes in the glass (Fig. 2) are arranged as ~ 60-µm thick coronas/halos/annuli around the vesicles. Assuming that each vesicle is surrounded by the same thickness of bubbly corona, the actual value of β relative to that determined in BSE imaging is augmented up to 0.04 in each experimental run product. If nanobubbles forming foams (Fig. 6) are highly deformable ($Ca >> 1$) as much as the microbubbles investigated in the run products of Pistone et al. (2017) (Figs. 1 and 3), the increased total porosity in the melt pool surrounded by

quartz crystals can promote an additional sample viscosity decrease up to half order of magnitude at large crystallinity ($\phi > 0.5$; Pistone et al. 2016b) at which gas bubbles already favour a decrease of magma viscosity of up to 4 orders of magnitude (Pistone et al. 2012, 2013), with consequent increased mobility of the magma ascending in the volcanic conduit.

At higher temperature (> 900 °C), bubble coalescence drives gas loss from the sample and the residual melt crystallises up to 50% at nanoscale (Fig. 5). As pointed out in previous works (Mujin and Nakamura 2014; Di Genova et al. 2017a; 2018; 2020a, b; Mujin et al. 2017; Cáceres et al. 2020, 2021), nanocrystallisation of the silicate melt increases both the viscosity of the silicate melt due to depletion of network-modifying elements (Fe, Ti, Mg, Ca) and concomitant increase of polymerizing elements (Si), and the viscosity of the whole system due to the increase of the nanolite cargo. In this case, the silicate melt viscosity increase is primarily augmented by H_2O loss via degassing and is expected to be larger than two orders of magnitude as previously stated (Di Genova et al. 2017a).

The increase of magma viscosity by the increasing amount of nanolites is difficult to quantify as we did not perform in situ viscosity measurements. Di Genova et al. (2020a, b) conducted viscosity measurements on analog materials made of silicon oil and suspended SiO_2 particles. Analog materials simulating certain physical aspects of magma properties are very helpful, but they are characterised by constant chemical and physical properties of the suspending liquid and fail to capture the geochemical changes of the melt composition caused by concomitant H_2O degassing and formation of nanolites, both favouring melt polymerisation as observed in high-resolution Raman spectroscopic analysis (Di Genova et al. 2017a, 2018; Cáceres et al. 2021). Subsequent experiments led by Di Genova et al. (2020b) have shown that agglomeration/clustering of nanocrystals and formation of high-viscosity shells around the newly formed nanolites can produce a tangible increase of magma viscosity up to one order of magnitude in proximity of the glass transition temperature. However, these experiments only capture the formation of nanocrystals upon temperature increase in absence of gas exsolution. In our experiments, we expect a rapid change of magma viscosity that first decreases with the increase of nanoporosity and, then increases due to the concomitant increase of nanolite volume fraction and silicate melt viscosity upon H_2O degassing.

Because the quantification of magma viscosity must account for such concomitant effects, the choice of the rheological model is crucial. Several models adopt the effective medium theory to reduce a three-phase flow to a two-phase system when either crystals or bubbles is consistently larger in size than the other, assuming that gas bubbles remain spherical and rigid during deformation ($Ca < 1$; Phan-Thien and Pham 1997; Harris and Allen III, 2008; Mader et al. 2013; Truby et al. 2015). For further details on the suitability of each rheological model, see the work of Pistone et al. (2016b) proposing an empirical three-phase magma rheology model that does not apply the effective medium theory.

The combination of experiments from Pistone et al. (2017) highlighting deformation of microbubbles, and the new STEM-based experiments showing nanoporosity forming microporosity via gas coalescence, suggests that H_2O-saturated silica-rich magmas (ranging from andesite to rhyolite) may experience an initial acceleration (up to 25%) due to the development of deformable nanoporosity that increases buoyancy and supports magma flow even at $\phi > 0.3$ (Pistone et al. 2016b). Conversely, if the nanoporosity is composed of rheologically rigid gas foams, this will favour an increase of magma viscosity (Llewellin and Manga 2005). In any case, during bubble coalescence triggered by a combination of gas expansion, shear deformation, and localised fracturing of melt films that favour magma outgassing (e.g., Tuffen et al. 2003; Okumura et al. 2010; Caricchi et al. 2011; Castro et al. 2012; Pistone et al. 2012; Shields et al. 2014, 2016) and densification (Vasseur et al. 2013; Wadsworth et al. 2014; Heap et al. 2015), the initial magma mobility is rapidly changed into a rheological stalling or jamming (Cates et al. 1998; Petford 2009) that would either halt the magma flow in the conduit (Pistone et al. 2013) or force the system to fragment violently (Sparks 1997; Papale 1999; Alidibirov and Dingwell 2000; Gonnermann and Manga 2003; Spieler et al. 2004).

Silicic volcanoes commonly exhibit alternating episodes of explosive and effusive activity during dome-forming eruptions (e.g., Matthews et al. 1997; Watts et al. 2002; Sherrod et al. 2008; Holland et al. 2011; Ogburn et al. 2012, 2015; Lamb et al. 2015; Wolpert et al. 2016) promoted by the ascent and extrusion of high-crystallinity systems ($\phi > 0.5$, including both phenocryst and microlite populations; Watts et al. 2002). Using the ongoing activity of La Soufriére in St. Vincent (Global Volcanism Program 2021) as an example of a dome-forming eruption, the volcano starts with a low volume effusion of a lava dome, accompanied by mild to vigorous outgassing on and around the pancake style dome. Then, the volcano can quite unexpectedly produce a very high-intensity explosive eruption. Such explosive events following the initially benign lava dome extrusion tend to occur after stages of unusual deflation and drain-back events of the dome body, which is thought to have sealed gas escape routes (Matthews et al. 1997; Watts et al. 2002; Simmons et al. 2005). This type of behaviour is interpreted as a result of H_2O degassing-induced crystallisation favouring the magma strength and internal overpressure increase, which both lead to system fragmentation (Matthews et al. 1997; Melnik and Sparks 1999).

Our results suggest a new alternative interpretation explaining how sudden explosive eruption may follow initially benign lava dome extrusion. Degassing forming macrobubbles, microbubbles, and nanobubbles allows lava domes to be gently extruded until the generation of permeable pathways for persistent gas escape promotes slow crystallisation of nanolites that rheologically lock the system, trap additional volatile inputs derived from larger depth, and make the lava dome a sort of pressure cooker that may blow up violently with consequent explosive volcanic activity. In this framework, nanolites anticipate chemical (Figs. 2 and 5) and physical changes of the residual melt (Figs. 3, 4, 5, 6 and 7) that have been generally correlated to microlite formation (Geschwind and Rutherford 1995; Hammer et al. 1999; Martel and Poussineau 2007; Noguchi et al. 2008; Cichy et al. 2011; Martel 2012). Microlites forming during magma ascent serve to exaggerate the changes introduced by nanolite formation, but nanoscale changes may in fact have a greater impact than what has been considered at microscale so far. The rheological effects at the two different scales are then cumulative.

Conclusions

In this study, we have explored degassing-induced crystallisation in situ and at nanoscale using a novel approach that combines secondary electron imaging and heating, to simulate decompression of felsic magma. We monitored the nanostructural changes in terms of formation of nanoporosity, deflation and removal of this nanoporosity via outgassing, and nanolite crystallisation. Such nanostructural changes help explain variations in the geochemical fingerprints of glasses from run products of Pistone et al. (2017) who explored the rheology of high crystallinity, hydrous dacite samples able to vesiculate during deformation at high temperature in a parallel-plate viscometer. The ability to image degassing and crystallisation at nanoscale reveals a sequence of complex physical and chemical changes of the residual melt. Studies at such high spatial resolution are crucial to unravel the impact of nanostructures on macroscale petrophysical and hydrodynamic properties (Garing et al. 2015, 2017; Hebert et al. 2015; Soulaine et al. 2016). This study indeed provides insights into the competition between gas retention and crystallisation, that modulates the ability of magma to ascend in a volcanic conduit, and may control the transition between effusive and explosive eruptions occurring in lava dome-forming volcanic activity. Specifically, we have detailed that degassing of felsic hydrous melts produces initial widespread nanoporosity, expected to decrease magma viscosity and enhance magma mobility even at high crystallinity. Then, with continuous degassing, nanolites form dense clusters in a H_2O-poor viscous melt that increase the viscosity, potentially slowing ascent and trapping residual exsolved gas, and keeping the magma gas-charged until its possible brittle fragmentation.

Supplementary Information The online version contains supplementary material available at https://doi.org/10.1007/s00410-022-01900-1.

Acknowledgements NSF EAR-1220051 to A.W., NSF EAR-1347248 to E.C., SNF PZ00P2_168166, PBEZP2_14922, P3000P2_154574, and UGA Presidential Funds to M.P., and ERC Advanced Grant CRITMAG to J.D. Blundy supported this research. We acknowledge: T. Gooding and A. Mansur (Smithsonian) for support during SEM analyses; T. Rose (Smithsonian), A. Trucco (University of Florida), C. Henderson (CAMECA) for support during EPMA analyses; Alberto Luisoni AG (Switzerland) and Nabaltec AG (Germany) for supplying quartz crystals and APYRAL 60CD used in the starting materials. The authors thank two anonymous reviewers for their insightul analysis of an earlier version of this contribution and G. Moore for editorial handling.

References

Alidibirov M, Dingwell DB (2000) Three fragmentation mechanisms for highly viscous magma under rapid decompression. J Volcanol Geotherm Res 100:413–421

Allabar A, Gross ES, Nowak M (2020) The effect of initial H_2O concentration on decompression induced phase separation and degassing of hydrous phonolitic melt. Contrib Mineral Petrol 2:1–19

Applegarth LJ, Tuffen HJ, Pinkerton MH, Cashman KV (2013) Direct observations of degassing induced crystallization in basalts. Geology 41:243–246

Ardia P, Giordano D, Schmidt MW (2008) A model for the viscosity of rhyolite as a function of H_2O-content and pressure: a calibration based on centrifuge piston cylinder experiments. Geochim Cosmochim Acta 72:6013–6123

Ardia P, Di Muro A, Giordano D, Massare D, Sanchez-Valle C, Schmidt MW (2014) Densification mechanisms of haplogranite glasses as a function of water content and pressure based on density and Raman data. Geochimica et Cosmochimica Acta 138:158–180

Armstrong JT (1988) Quantitative analysis of silicate and oxide materials: comparison of Monte Carlo ZAF and ψ (ρz) procedures. In: Newbury DE (ed) Microbeam analysis. San Francisco Press Inc, San Francisco, CA, pp 239–246

Arzilli F, Carroll M (2013) Crystallization kinetics of alkali feldspars in cooling and decompression-induced crystallization experiments in trachytic melt. Contrib Mineral Petrol 166:1011–1027

Bachmann O, Bergantz GW (2004) On the origin of crystal-poor rhyolites: extracted from batholitic crystal mushes. J Petrol 45:1565–1582

Bagdassarov NS, Dingwell DB, Wilding MC (1996) Rhyolite magma degassing: an experimental study of melt vesiculation. Bull Volcanol 57:587–601

Balashov N, Zaraisky GP, Seltmann R (2000) Fluid-magmatic interaction and oscillation phenomena during granite melt crystallization with water-fluoride fluid gain-loss. Petrologiya 8:563–585

Barmin A, Melnik O, Sparks RSJ (2002) Periodic behavior in lava dome eruptions. Earth Planet Sci Lett 199:173–184

Befus KS (2016) Crystallization kinetics of rhyolitic melts using oxygen isotope ratios. Geophys Res Lett. https://doi.org/10.1002/2015GL067288

Befus KS, Andrews BJ (2018) Crystal nucleation and growth produced by continuous decompression of Pinatubo magma. Contrib Mineral Petrol. https://doi.org/10.1007/s00410-018-1519-5
Bikerman JJ (1973) Foams. Springer, Berlin, Heidelberg, New York
Binder K (2015) Demixing. In: Li D (ed) Encyclopedia of microfluidics and nanofluidics. Springer, New York, pp 537–553
Binder K, Stauffer D (1974) Theory for the slowing down of the relaxation and spinodal decomposition of binary mixtures. Phys Rev Lett 33:1006–1009
Blatter D, Carmichael I (1998) Plagioclase-free andesites from Zitácuaro (Michoacán), Mexico: petrology and experimental constraints. Contrib Mineral Petrol 132:121–138
Blatter D, Carmichael I (2001) Hydrous phase equilibria of a Mexican high-silica andesite: a candidate for a mantle origin? Geochim Cosmochim Acta 65:4043–4065
Blatter D, Carmichael I, Deino A, Renne P (2001) Neogene volcanism at the front of the central Mexican volcanic belt: basaltic andesites to dacites, with contemporaneous shoshonites and high-TiO_2 lavas. Geol Soc Am Bull 113:1324–1342
Blower JD (2001) Factors controlling permeability-porosity relationships in magma. Bull Volcanol 63:497–504
Blower JD, Mader HM, Wilson SDR (2001) Coupling of viscous and diffusive controls on bubble growth during explosive volcanic eruptions. Earth Planet Sci Lett 193:47–56
Blundy JD, Sparks RSJ (1992) Petrogenesis of mafic inclusions in granitoids of the Adamello Massif, Italy. J Petrol 33:1039–1104
Blundy J, Cashman K, Humphreys M (2006) Magma heating by decompression-driven crystallization beneath andesite volcanoes. Nature 443:76–80
Brugger C, Hammer J (2010) Crystallization kinetics in continuous decompression experiments: implications for interpreting natural magma ascent processes. J Petrol 51:1941–1965
Burgisser A, Gardner JE (2005) Experimental constraints on degassing and permeability in volcanic conduit flow. Bull Volcanol 67:42–56
Burgisser A, Chevalier L, Gardner JE, Castro JM (2017) The percolation threshold and permeability evolution of ascending magmas. Earth Planet Sci Lett 470:37–47
Byerly GR, Melson WG, Nelen J, Jarosewich E (1977) Abyssal volcanic glasses as indicators of magma compositions. Smithson Contrib Earth Sci 19:22–29
Cabrera A, Weinberg RF, Wright HMN, Zlotnik S, Cas RAF (2010) Melt fracturing and healing: a mechanism for degassing and origin of silicic obsidian. Geology 39:67–70
Cáceres F, Wadsworth FB, Scheu B, Colombier M, Madonna C, Cimarelli C, Hess K-U, Kaliwoda M, Ruthensteiner B, Dingwell DB (2020) Can nanolites enhance eruption explosivity? Geology 48:997–1001
Cáceres F, Scheu B, Hess K-U, Cimarelli C, Vasseur J, Kaliwoda M, Dingwell DB (2021) From melt to crystals: the effects of cooling on Fe–Ti oxide nanolites crystallisation and melt polymerisation at oxidising conditions. Chem Geol 563:120057
Cahn JW (1961) On spinodal decomposition. Acta Metal 9:795–801
Cann JR (1970) Upward movement of granitic magma. Geol Mag 107:335–340
Caricchi L, Pommier A, Pistone M, Castro J, Burgisser A, Perugini D (2011) Strain-induced magma degassing: insights from simple-shear experiments on bubble bearing melts. Bull Volcanol 73:1245–1257
Cashman KV (1992) Groundmass crystallization of Mount St. Helens dacite, 1980–1986: a tool for interpreting shallow magmatic processes. Contrib Miner Petrol 109:431–449
Cashman KV, Blundy JD (2000) Degassing and crystallization of ascending andesite. Philos Trans R Soc 358:1487–1513
Castro J, Manga M, Martin M (2005) Vesiculation rates of obsidian domes inferred from H_2O concentration profiles. Geophys Res Lett 32:L21307
Castro J, Beck P, Tuffen H, Nichols A, Dingwell DB, Martin M (2008) Timescales of spherulite crystallization in obsidian inferred from water concentration profiles. Am Miner 93:1816–1822
Castro JM, Cordonnier B, Tuffen H, Tobin MJ, Puskar L, Martin MC, Bechtel HA (2012) The role of melt-fracture degassing in defusing explosive rhyolite eruptions at Volcán Chaitén. Earth Planet Sci Lett 333–334:63–69
Cates ME, Wittmer JP, Bouchauad J-P, Claudin P (1998) Jamming, force chains and fragile matter. Phys Rev Lett 81:1841–1844
Cazaux J (1996) Electron probe microanalysis of insulating materials: quantification problems and some possible solutions. X-Ray Spectrom 25:265–280
Cichy S, Botcharnikov R, Holtz F, Behrens H (2011) Vesiculation and microlite crystallization induced by decompression: a case study of the 1991–1995 Mt. Unzen eruption (Japan). J Petrol 52:1469–1492
Colombier M, Wadsworth FB, Gurioli L, Scheu B, Kueppers U, Di Muro A, Dingwell DB (2017) The evolution of pore connectivity in volcanic rocks. Earth Planet Sci Lett 462:99–109
Cormier L (2014) Nucleation in glasses - new experimental findings and recent theories. Procedia Mater Sci 7:60–71
Cottrell E, Lanzirotti A, Mysen B, Birner S, Kelley KA, Botcharnikov R, Davis FA, Newville M (2018) A Mössbauer-based XANES calibration for hydrous basalt glasses reveals radiation-induced oxidation of Fe. Am Mineral 103:489–501
Couch S, Sparks RSJ, Carroll MR (2003) The kinetics of degassing-induced crystallization at Soufrière hills volcano, Montserrat. J Petrol 44:1477–1502
Deubener J, Allix M, Davis MJ, Duran A, Höche T, Honma T, Komatsu T, Krüger S, Mitra I, Müller R, Nakane S, Pascual MJ, Schmelzer JWP, Zanotto ED, Zhou S (2018) Updated definition of glass-ceramics. J Non-Crystalline Solids 501:3–10
Devine JD, Gardner JE, Brack HP, Layne GD, Rutherford MJ (1995) Comparison of microanalytical methods for estimating H_2O contents of silicic volcanic glasses. Am Mineral 80:319–328
Di Genova D, Sicola S, Romano C, Vona A, Fanara S, Spina L (2017a) Effect of iron and nanolites on Raman spectra of volcanic glasses: a reassessment of existing strategies to estimate the water content. Chem Geol 475:76–86
Di Genova D, Kolzenburg S, Wiesmaier S, Dallanave E, Neuville DR, Hess K-U, Dingwell DB (2017b) A chemical tipping point governing mobilization and eruption style of rhyolitic magma. Nature 552:235–238
Di Genova D, Caracciolo A, Kolzenburg S (2018) Measuring the degree of "nanotilization" of volcanic glasses: understanding syn-eruptive processes recorded in melt inclusions. Lithos 318–319:209–218
Di Genova D, Brooker RA, Mader HM, Drewitt JWE, Longo A, Deubener J, Neuville DR, Fanara S, Shebanova O, Anzellini S, Arzilli F, Bamber EC, Hennet L, La Spina G, Miyajima N (2020a) In situ observation of nanolite growth in volcanic melt: a driving force for explosive eruptions. Sci Adv 6:eabb0413
Di Genova D, Zandona A, Deubener J (2020b) Unravelling the effect of nano-heterogeneity on the viscosity of silicate melts: implications for glass manufacturing and volcanic eruptions. J Non-Cryst Solids 545:120248. https://doi.org/10.1016/j.jnoncrysol.2020.120248
Dingwell DB, Webb SL (1989) Structural relaxation in silicate melts and non-Newtonian melt rheology in geologic processes. Phys Chem Miner 16:508–516

Dubosq R, Pleše P, Langelier B, Gault B, Schneider D (2021) Bubbles and element clusters in rock melts: a chicken and egg problem. EGU General Assembly 2021, pp EGU21–EGU60

Eichelberger JC, Carrigan CR, Westrich HR, Price RH (1986) Non-explosive silicic volcanism. Nature 323:598–602

Farquharson J, Heap MJ, Varley NR, Baud P, Reuschlé T (2015) Permeability and porosity relationships of edifice-forming andesites: a combined field and laboratory study. J Volcanol Geotherm Res 297:52–68

Farquharson JI, Heap MJ, Lavallée Y, Varley NR, Baud P (2016) Evidence for the development of permeability anisotropy in lava domes and volcanic conduits. J Volcanol Geotherm Res 323:163–185

Gaonac′h, H, Lovejoy S, Schertzer D (2003) Percolating magmas and explosive volcanism. Geophys Res Lett 30(11):1559. https://doi.org/10.1029/2002GL016022

Garboczi EJ, Snyder KA, Douglas JF, Thorpe MF (1995) Geometrical percolation threshold of overlapping ellipsoids. Phys Rev E 52:819–828

Gardner JE (2007) Bubble coalescence in rhyolitic melts during decompression from high pressure. J Volcanol Geotherm Res 166:161–176

Gardner JE, Befus KS, Watkins JM, Clow T (2016) Nucleation rates of spherulites in natural rhyolitic lava. Am Miner 101:2367–2376

Garing C, Gouze P, Kassab M, Riva M, Guadagnini A (2015) Anti-correlated porosity-permeability changes during the dissolution of carbonate rocks: experimental evidences and modelling. Transp Porous Med 107:595–621

Garing C, de Chalendar JA, Voltolini M, Ajo-Franklin JB, Benson SM (2017) Pore-scale capillary pressure analysis using multi-scale X-ray micromotography. Adv Water Resour 104:223–241

Gaunt HE, Sammonds PR, Meredith PG, Smith R, Pallister JS (2014) Pathways for degassing during the lava dome eruption of Mount St. Helens 2004–2008. Geology 2014:947–950

Geschwind CH, Rutherford MJ (1995) Crystallization of microlites during magma ascent: the fluid mechanics of 1980–1986 eruptions of Mt St Helens. Bull Volcanol 57:356–370

Giachetti T, Gonnermann HM, Gardner JE, Burgisser A, Hajimirza S, Earley TC, Truong N, Toledo P (2019) Bubble coalescence and percolation threshold in expanding rhyolitic magma. Geochem, Geophys, Geosyst 20:1054–1074

Giordano D, Russell JK, Dingwell DB (2008) Viscosity of magmatic liquids: a model. Earth Planet Sci Lett 271:123–134

Giordano D, Vona A, Gonzalez-Garcia D, Allabar A, Kolzenburg S, Polo L, de Janasi Assis V, Behrens H, De Campos CP, De Cristofaro S, Guimaraes Freitas L, Nowak M, Müller D, Günther A, Masotta M, Roverato M, Romano C, Dingwell DB (2021) Viscosity of Palmas-type magmas of the Paraná magmatic province (Rio Grande do Sul State, Brazil): implications for high-temperature silicic volcanism. Chem Geol 560:119981. https://doi.org/10.1016/j.chemgeo.2020.119981

Girona T, Costa F, Newhall C, Taisne B (2014) On depressurization of volcanic magma reservoirs by passive degassing. J Geophys Res Solid Earth 119:8667–8687

Glazner AF (2019) The ascent of water-rich magma and decompression heating: a thermodynamic analysis. Am Mineral 104:890–896

Global Volcanism Program (2021) Volcanoes of the world: v. 4.5.0. In: Venzke E (ed) Smithsonian Institution, Downloaded 22 Apr 2021. https://doi.org/10.5479/si.GVP.VOTW4-2013.

Gonnermann HM, Manga M (2003) Explosive volcanism may not be an inevitable consequence of magma fragmentation. Nature 426:432–435

Gonnermann HM, Giachetti T, Fliedner C, Nguyen CT, Houghton BF, Crozier JA, Carey RJ (2017) Permeability during magma expansion and compaction: observations and experiments. J Geophys Res Solid Earth 122:9825–9848

González-García D, Giordano D, Allabar A, Andrade FRD, Polo LA, Janasi VA, Lucchetti ACF, Hess K-U, De Campos C, Dingwell DB (2021) Retrieving dissolved H_2O content from micro-Raman spectroscopy on nanolitized silicic glasses: application to volcanic products of the Paraná magmatic province, Brazil. Chem Geol 567:120058. https://doi.org/10.1016/j.chemgeo.2021.120058

Hajimirza S, Gonnermann HM, Gardner JE (2021) Reconciling bubble nucleation in explosive eruptions with geospeedometers. Nat Commun 12:1–8

Hammer JE, Rutherford MJ (2002) An experimental study of decompression-induced crystallization in silicic melt. J Geophys Res 107:8–24

Hammer JE, Cashman KV, Hoblitt RP, Newman S (1999) Degassing and microlite crystallization during pre-climactic events of the 1991 eruption of Mt. Pinatubo, Philippines. Bull Volcanol 60:355–380

Harris PG, Kennedy WQ, Scarfe CM (1970) Volcanism versus plutonism— the effect of chemical composition. In: Newall G, Rast N (eds) Mechanism of igneous intrusion. Liverpool Geological Society, UK, pp 187–200

Heap MJ, Farquharson JI, Wadsworth FB, Kolzenburg S, Russell JK (2015) Timescales for permeability reduction and strength recovery in densifying magma. Earth Planet Sci Lett 429:223–233

Hebert V, Garing C, Luquot L, Pezard PA, Gouze P (2015) Multi-scale X-ray tomography analysis of carbonate porosity. Geol Soc Lond-Spec Publ 406:61–79

Hess K-U, Dingwell DB (1996) Viscosities of hydrous leucogranitic melts: a non-Arrhenian model. Am Mineral 81:1297–1300

Hoblitt RP, Harmon RS (1993) Bimodal density distribution of cryptodome dacite from the 1980 eruption of Mt. St. Helens, Washington. Bull Volcanol 55:421–437

Höche T, Mäder M, Bhattacharyya S, Henderson GH, Gemming T, Wurth R, Rüssel C, Avramov I (2011) $ZrTiO_4$ crystallisation in nanosized liquid-liquid phase-separation droplets in glass-a quantitative XANES study. CrystEngComm 13:2550–2556

Holland ASP, Watson IM, Phillips JC, Caricchi L (2011) Degassing processes during lava dome growth: insights from Santiaguito lava dome, Guatemala. J Volcanol Geotherm Res 202:153–166

Hort M (1998) Abrupt change in magma liquidus temperature because of volatile loss or magma mixing: effects on nucleation, crystal growth and thermal history of the magma. J Petrol 39:1063–1076

Hughes EC, Buse B, Kearns SL, Blundy JD, Kilgour G, Mader HM, Brooker RA, Blazer B, Botcharnikov RE, Di Genova D, Almeev RR, Riker JM (2018) High spatial resolution analysis of the iron oxidation state in silicate glasses using the electron probe. Am Mineral 103:1473–1486

Hughes EC, Buse B, Kearns SL, Blundy JD, Mader HM, Carlo M (2019) Low analytical totals in EPMA of hydrous silicate glass due to sub-surface charging: obtaining accurate volatiles by difference. Chem Geol 505:48–56

Hui HJ, Zhang YX, Xu ZJ, Del Gaudio P, Behrens H (2009) Pressure dependence of viscosity of rhyolitic melts. Geochim Cosmochim Acta 73:3680–3693

Ichihara M, Kameda M (2004) Propagation of acoustic waves in a visco-elastic two-phase system: influences of the liquid viscosity and the internal diffusion. J Volcanol Geotherm Res 137:1–3

Jarosewich E (2002) Smithsonian microbeam standards. J Res Nat Inst Stand Technol 107:681–685

Johannes WJ, Holtz F (1996) Petrogenesis and experimental petrology of granitic rocks. Springer, p 335

Johnson ER, Wallace PJ, Cashman KV, Delgado-Granados H, Kent AJR (2008) Magmatic volatile contents and degassing-induced crystallization at Volcán Jorullo, Mexico: implications for melt evolution and the plumbing systems of monogenetic volcanoes. Earth Planet Sci Lett 269:477–486

Karlstrom L, Dunham EM (2016) Excitation and resonance of acoustic-gravity waves in a column of stratified, bubbly magma. J Fluid Mech 797:431–470

Kleebusch E, Patzig C, Höche T, Rüssel C (2018) The evidence of phase separation droplets in the crystallization process of a Li_2O-Al_2O_3-SiO_2 glass with TiO_2 as nucleating agent - an X-ray diffraction and (S)TEM-study supported by EDX-analysis. Ceram Int 44:2919–2926

Kleest C, Webb SL, Fanara S (2020) Rheology of melts from the colli albani volcanic district (Italy): a case study. Contrib Mineral Petrol. https://doi.org/10.1007/s00410-020-01720-1

Klug C, Cashman KV (1996) Permeability development in vesiculating magmas: implications for fragmentation. Bull Volcanol 58:87–100

Kraynik AM (1988) Foam flows. Annu Rev Fluid Mech 20:325–357

Kurzon I, Lyakhovsky V, Navon O, Chouet B (2011) Pressure waves in a supersaturated bubbly magma. Geophys J Int 187:421–438

Kushnir AR, Martel C, Champallier R, Arbaret L (2017) In situ confirmation of permeability development in shearing bubble-bearing melts and implications for volcanic outgassing. Earth Planet Sci Lett 458:315–326

Lamb OD, De Angelis S, Umakoshi K, Hornby AJ, Kendrick JE, Lavallée Y (2015) Cyclic fracturing during spine extrusion at Unzen volcano, Japan. Solid Earth 7:2109–2149

Lavallée Y, Dingwell DB, Johnson JB, Cimarelli C, Hornby AJ, Kendrick JE, Von Aulock FW, Kennedy BM, Andrews BJ, Wadsworth FB, Rhodes E, Chigna G (2015) Thermal vesiculation during volcanic eruptions. Nature 528:544–547

Lindoo A, Larsen JF, Cashman KV, Oppenheimer J (2017) Crystal controls on permeability development and degassing in basaltic andesite magma. Geol 45:831–834. https://doi.org/10.1130/G39157.1

Le Maitre RW, Streckeisen A, Zanettin B, Le Bas MJ, Bonin B, Bateman P, Bellieni DA, Efremova S, Keller J, Lameyre J, Sabine PA, Schmid R, Sørensen H, Woolley AR (2002) Igneous rocks: a classification and glossary of terms, recommendations of the international union of geological sciences, subcommission of the systematics of igneous rocks. Cambridge University Press (**ISBN 0-521-66215-X**)

Lipman P, Banks N, Rhodes J (1985) Degassing-induced crystallization of basaltic magma and effects on lava rheology. Nature 317:604–607

Llewellin EW, Manga M (2005) Bubble suspension rheology and implications for conduit flow. J Volcanol Geotherm Res 143:205–217

Llewellin EW, Mader HM, Wilson SDR (2002) The rheology of a bubbly liquid. Proc R Soc London A 458:987–1016

Mader HM, Llewellin EW, Mueller SP (2013) The rheology of two-phase magmas: a review and analysis. J Volcanol Geotherm Res 257:135–158

Mandeville CW, Carey S, Sigurdsson H (1996) Magma mixing, fractional crystallization and volatile degassing during the 1883 eruption of Krakatau volcano, Indonesia. J Volcanol Geotherm Res 74:243–274

Mandeville C, Webster J, Rutherford M, Taylor B, Timbal A, Faure K (2002) Determination of molar absorptivities for infrared absorption bands of H_2O in andesitic glasses. Am Mineral 87:813–821

Marsh BD (1981) On the crystallinity, probability of occurrence, and rheology of lava and magma. Contrib Mineral Petrol 78:85–98

Martel C (2012) Eruption dynamics inferred from microlite crystallization experiments: application to plinian and dome-forming eruptions of Mt. Pelee (Martinique, Lesser Antilles). J Petrol 53:699–725

Martel C, Iacono-Marziano G (2015) Timescales of bubble coalescence, outgassing, and foam collapse in decompressed rhyolitic melts. Earth Planet Sci Lett 412:173–185

Martel C, Poussineau S (2007) Diversity of eruptive style inferred from the microlites of Mt. Pelée andesite (Martinique, Lesser Antilles). J Volcanol Geotherm Res 166:233–254

Martel C, Schmidt B (2003) Decompression experiments as an insight into ascent rates of silicic magmas. Contrib Mineral Petrol 144:397–415

Martula DS, Hasegawa T, Lloyd DR, Bonnecaze RT (2000) Coalescence-induced coalescence of inviscid droplets in a viscous fluid. J Colloid Interface Sci 232:241–253

Matthews SJ, Gardeweg MC, Sparks RSJ (1997) The 1984 to 1996 cyclic activity of Lascar Volcano, northern Chile: cycles of dome growth, dome subsidence, degassing and explosive eruptions. Bull Volcanol 59:72–82

McIntosh IM, Llewellin EW, Humphreys MCS, Nichols ARL, Burgisser A, Schipper CI, Larsen JF (2014) Distribution of dissolved water in magmatic glass records growth and resorption of bubbles. Earth Planet Sci Lett 401:1–11

McKenzie DP, Bickle MJ (1988) The volume and composition of melt generated by extension of the lithosphere. J Petrol 29:625–679

Melnik O, Sparks RSJ (1999) Nonlinear dynamics of lava dome extrusion. Nature 402:37–41

Melnik O, Lyakhovsky V, Shapiro NM, Galina N, Bergal-Kuvikas O (2020) Deep long period volcanic earthquakes generated by degassing of volatile-rich basaltic magmas. Nat Commun 11:3918. https://doi.org/10.1038/s41467-020-17759-4

Melson WG, O'Hearn T, Jarosewich E (2002) A data brief on the Smithsonian Abyssal volcanic glass data file. Geochem Geophys Geosyst. https://doi.org/10.1029/2001GC000249

Mollard E, Martel C, Bourdier J (2012) Decompression-induced crystallization in hydrated silica-rich melts: empirical models of experimental plagioclase nucleation and growth kinetics. J Petrol 53:1743–1766

Moore G, Carmichael I (1998) The hydrous phase equilibira (to 3 kbar) of an andesite and basaltic andesite from western Mexico: constraints on water content and conditions of phenocryst growth. Contrib Mineral Petrol 130:304–319

Morgan GB, London D (1996) Optimizing the electron microprobe analysis of hydrous alkali aluminosilicate glasses. Am Mineral 81:1176–1185

Mueller S, Melnik O, Spieler O, Scheu B, Dingwell DB (2005) Permeability and degassing of dome lavas undergoing rapid decompression: an experimental determination. Bull Volcanol 67:526–538

Mueller S, Scheu B, Spieler O, Dingwell DB (2008) Permeability control on magma fragmentation. Geology 36:399–402

Mueller S, Scheu B, Kueppers U, Spieler O, Richard D, Dingwell DB (2011) The porosity of pryoclasts as an indicator of volcanic explosivity. J Volcanol Geotherm Res 203:168–174

Mujin M, Nakamura M (2014) A nanolite record of eruption style transition. Geology 42:611–614

Mujin M, Nakamura M, Miyake A (2017) Eruption style and crystal size distributions: crystallization of groundmass nanolites in the 2011 Shinmoedake eruption. Am Mineral 102:2367–2380

Namiki A, Manga M (2008) Transition between fragmentation and permeable outgassing of low viscosity magmas. J Volcanol Geotherm Res 169:48–60

Nguyen CT, Gonnermann HM, Houghton BF (2014) Explosive to effusive transition during the largest volcanic eruption of the 20th century (Novarupta 1912, Alaska). Geol 42:703–706. https://doi.org/10.1130/G35593.1

Nguyen CT, Gonnermann HM, Chen Y, Huber C, Maiorano AA, Gouldstone A, Dufek J (2013) Film drainage and the lifetime of bubbles. Geochem Geophys, Geosyst 14:3616–3631

Noguchi S, Toramaru A, Nakada S (2008) Relation between microlite textures and discharge rate during the 1991–1995 eruptions at Unzen, Japan. J Volcanol Geotherm Res 175:141–155

Ogburn SE, Loughlin SC, Calder ES (2012) DomeHaz: dome-forming eruptions database v2.4. On Vhub at https://vhub.org/groups/domedatabase.

Ogburn SE, Loughlin SC, Calder ES (2015) The association of lava dome growth with major explosive activity (VEI ≥ 4): DomeHaz, a global dataset. Bull Volcanol. https://doi.org/10.1007/s00445-015-0919-x

Okumura S, Nakamura M, Tsuchiyama A (2006) Shear-induced bubble coalescence in rhyolitic melts with low vesicularity. Geophys Res Lett 33:L20316. https://doi.org/10.1029/2006GL027347

Okumura S, Nakamura M, Nakano T, Uesugi K, Tsuchiyama A (2010) Shear deformation experiments on vesicular rhyolite: implications for brittle fracturing, degassing, and compaction of magmas in volcanic conduits. J Geophys Res 115:B06201. https://doi.org/10.1029/2009JB006904

Papale P (1999) Strain-induced magma fragmentation in explosive eruptions. Nature 397:425–428

Petford N (2009) Which effective viscosity? Mineral Mag 73:167–191

Phan-Thien N, Pham DC (1997) Differential multiphase models for polydispersed suspensions and particulate solids. J Non-Newton Fluid Mech 72:305–318

Pistone M, Caricchi L, Ulmer P, Burlini L, Ardia P, Reusser E, Marone F, Arbaret L (2012) Deformation experiments of bubble- and crystal-bearing magmas: rheological and microstructural analysis. J Geophys Res. https://doi.org/10.1029/2011JB008986

Pistone M, Caricchi L, Ulmer P, Burlini L, Reusser E, Ardia P (2013) Rheology of volatile-bearing crystal mushes: mobilization vs. viscous death. Chem Geol 345:16–39

Pistone M, Caricchi L, Fife JL, Mader K, Ulmer P (2015a) In situ X-ray tomographic microscopy observations of vesiculation of bubble-free and bubble-bearing magmas. Bull Volcanol. https://doi.org/10.1007/s00445-015-0992-1

Pistone M, Arzilli F, Dobson KJ, Cordonnier B, Reusser E, Ulmer P, Marone F, Whittington AG, Mancini L, Fife JL, Blundy JD (2015b) Gas-driven filter pressing in magmas: insights into in-situ melt segregation from crystal mushes. Geology 43:699–702

Pistone M, Blundy JD, Brooker RA, EIMF (2016a) Textural and chemical consequences of interaction between hydrous mafic and felsic magmas: an experimental study. Contrib Mineral Petrol. https://doi.org/10.1007/s00410-015-1218-4

Pistone M, Cordonnier B, Ulmer P, Caricchi L (2016b) Rheological flow laws for multiphase magmas: an empirical approach. J Volcanol Geotherm Res 321:158–170

Pistone M, Whittington AG, Andrews BJ, Cottrell E (2017) Crystal-rich lava dome extrusion during vesiculation: an experimental study. J Volcanol Geotherm Res 347:1–14

Polacci M, Baker DR, Bai LP, Mancini L (2008) Large vesicles record pathways of degassing at basaltic volcanoes. Bull Volcanol 70:1023–1029

Proussevitch AA, Sahagian DL, Anderson AT (1993) Stability of foams in silicate melts. J Volcanol Geotherm Res 59:161–178

Riker J, Blundy J, Rust A, Botcharnikov R, Humphreys M (2015a) Experimental phase equilibria of a Mount St. Helens rhyodacite: a framework for interpreting crystallization paths in degassing silicic magmas. Contrib Mineral Petrol 170:1–22

Riker J, Cashman KV, Rust AC, Blundy JD (2015b) Experimental constraints on plagioclase crystallization during H_2O- and H_2O-CO_2-saturated magma decompression. J Petrol 56:1967–1998

Romine WL, Whittington AG (2015) A simple model for the viscosity of rhyolites as a function of temperature, pressure and water content. Geochim Cosmochim Acta 170:281–300

Rust AC, Cashman KV (2011) Permeability controls on expansion and size distributions of pyroclasts. J Geophys Res 116:B11202. https://doi.org/10.1029/2011JB008494

Rust AC, Cashman KV (2004) Permeability of vesicular silicic magma: inertial and hysteresis effects. Earth Planet Sci Lett 228:93–107

Saar MO, Manga M (1999) Permeability-porosity relationship in vesicular basalts. Geophys Res Lett 26:111–114

Saar MO, Manga M (2002) Continuum percolation threshold for randomly oriented soft-core prisms. Phys Rev E: Stat Nonlinear, Soft Matter Phys. https://doi.org/10.1103/PhysRevE.65.056131

Sahimi M (1994) Applications of percolation theory. Taylor and Francis, London, UK

Schiavi F, Bolfan-Casanova N, Withers AC, Médard E, Laumonier M, Laporte D, Flaherty T, Gómez-Ulla A (2018) Water quantification in silicate glasses by Raman spectroscopy: correcting for the effects of confocality, density and ferric iron. Chem Geol 483:312–331

Schipper CI, Castro JM, Tuffen H, James MR, How P (2013) Shallow vent architecture during hybrid explosive–effusive activity at Cordón Caulle (Chile, 2011–12): evidence from direct observations and pyroclast textures. J Volcanol Geotherm Res 262:25–37

Sharp TG, Stevenson RJ, Dingwell DB (1996) Microlites and "nanolites" in rhyolitic glass: microstructural and chemical characterization. Bull Volcanol 57:631–640

Shea T (2017) Bubble nucleation in magmas: a dominantly heterogeneous process? J Volcanol Geotherm Res 343:155–170

Sherrod D, Scott W, Stauer P (2008) A volcano rekindled: the renewed eruption of Mount St. Helens, 2004–2006, United States Geological Survey, Professional Paper, v. 1750.

Shields J, Mader HM, Pistone M, Caricchi L, Floess D, Putlitz B (2014) Strain-induced outgassing of three-phase magmas during simple shear. J Geophys Res. https://doi.org/10.1002/2014JB011111

Shields J, Mader HM, Caricchi L, Tuffen H, Mueller SP, Pistone M, Baumgartner L (2016) Unravelling textural heterogeneity in obsidian: shear-induced outgassing in the Rocche Rosse flow. J Volcanol Geotherm Res 310:137–158

Simmons J, Elsworth D, Voight B (2005) Classification and idealized limit-equilibrium analyses of dome collapses at Soufrière Hills volcano, Montserrat, during growth of the first lava dome: November 1995–March 1998. J Volcanol Geotherm Res 139(3–4):241–258. https://doi.org/10.1016/j.jvolgeores.2004.08.009

Soulaine C, Gjetvaj F, Garing C, Roman S, Russian A, Gouze P, Tchelepi HA (2016) The impact of sub-resolution porosity of X-ray microtomography images on the permeability. Transp Porous Media 113:227–243

Sparks RSJ (1997) Causes and consequences of pressurization in lava dome eruptions. Earth Planet Sci Lett 150:177–189

Sparks RSJ, Pinkerton H (1978) Effect of degassing on rheology of basaltic lava. Nature 276:385–386

Spieler O, Dingwell DB, Alidibirov M (2004) Magma fragmentation speed: an experimental determination. J Volcanol Geotherm Res 129:109–123

Stauffer D, Aharony A (1994) Introduction to percolation theory, 2nd edn. Taylor and Francis, London, UK, p 181

Swanson SE, Naney MT, Westrich HR, Eichelberger JC (1989) Crystallization history of Obsidian Dome, Inyo Domes, California. Bull Volcanol 51:161–176

Taisne B, Jaupart C (2008) Magma degassing and intermittent lava dome growth. Geophys Res Lett. https://doi.org/10.1029/2008GL035432

Takeuchi S, Nakashima S, Tomiya A, Shinohara H (2005) Experimental constraints on the low gas permeability of vesicular magma during decompression. Geophys Res Lett 32:L10312. https://doi.org/10.1029/2005GL022491

Tisato N, Quintal B, Chapman S, Podladchikov Y, Burg JP (2015) Bubbles attenuate elastic waves at seismic frequencies: first experimental evidence. Geophys Res Lett 42:3880–3887

Truby JM, Mueller SP, Llewellin EW, Mader HM (2015) The rheology of three-phase suspensions at low bubble capillary number. Proc R Soc Lond A. https://doi.org/10.1098/rspa.2014.0557

Tuffen H, Dingwell DB, Pinkerton H (2003) Repeated fracture and healing of silicic magma generate flow banding and earthquakes? Geology 31:1089–1092

Tuttle OF, Bowen NL (1958) Origin of granite in the light of experimental studies in the system $NaAlSi_3O_8$–$KAlSi_3O_8$–SiO_2–H_2O. Geol Soc Am Mem 74:153

van der Laan SR, Wyllie PJ (1993) Experimental interaction of granitic and basaltic magmas and implications for mafic enclaves. J Petrol 34:491–517

Vasseur J, Wadsworth FB (2017) Sphere models for pore geometry and fluid permeability in heterogeneous magmas. Bull Volcanol 79:77–92

Vasseur J, Wadsworth FB, Lavallée Y, Hess K-U, Dingwell DB (2013) Volcanic sintering: timescales of viscous densification and strength recovery. Geophys Res Lett. https://doi.org/10.1002/2013GL058105

Vasseur J, Wadsworth FB, Dingwell DB (2020) Permeability of polydisperse magma foam. Geology. https://doi.org/10.1130/G47094.1

Villeneuve N, Neuville DR, Boivin P, Bachèlery P, Richet P (2008) Magma crystallization and viscosity: a study of molten basalts from the Piton de la Fournaise volcano (La Réunion island). Chem Geol 256:242–251

Vogt PR, Byerly GR (1976) Magnetic anomalies and basalt composition in the Juan de Fuca-Gorda ridge area. Earth Planet Sci Lett 33:185–300

Wadsworth FB, Vasseur J, von Aulock FW, Hess K-U, Scheu B, Lavallée Y, Dingwell DB (2014) Nonisothermal viscous sintering of volcanic ash. J Geophys Res 119:8792–8804

Wadsworth FB, Vasseur J, Scheu B, Kendrick JE, Lavallée Y, Dingwell DB (2016) Universal scaling of fluid permeability during volcanic welding and sediment diagenesis. Geology 44:219–222

Walsh SDC, Saar MO (2008) Magma yield stress and permeability: insights from multiphase percolation theory. J Volcanol Geotherm Res 177:1011–1019

Waters LE, Andrews BJ, Lange RA (2015) Rapid crystallization of plagioclase phenocrysts in silicic melts during fluid-saturated ascent: phase equilibrium and decompression experiments. J Petrol 56:981–1006

Watkins J, Manga M, Huber C, Martin M (2009) Diffusion-controlled spherulite growth in obsidian inferred from H_2O concentration profiles. Contrib Mineral Petrol 157:163–172

Watts RB, Herd RA, Sparks RSJ, Young SR (2002) Growth patterns and emplacement of the andesitic lava dome at Soufrière hills volcano, Montserrat. Geol Soc Lond 21:115–152

Whittington AG, Hellwig BM, Behrens H, Joachim B, Stechern A, Vetere F (2009) The viscosity of hydrous dacitic liquids: implications for the rheology of evolving silicic magmas. Bull Volcanol 71:185–199

Wieczorek M, Zuber M, Phillips R (2001) The role of magma buoyancy on the eruption of lunar basalts. Earth Planet Sci Lett 185:71–83

Wolpert RL, Ogburn SE, Calder ES (2016) The longevity of lava dome eruptions. J Geophys Res 121:676–686

Wright TL, Fiske RS (1971) Origin of the differentiated and hybrid lavas of Kilauea volcano, Hawaii. J Petrol 12:1–65

Wright TL, Okamura RT (1977) Cooling and crystallization of tholeiitic basalt, 1965 Makaopuhi lava lake, Hawaii. USGS Professional Paper 1004: 1–78

Wright TL, Kinoshita WT, Peck DL (1968) March 1965 eruption of Kilauea volcano and the formation of Makaopuhi lava lake. J Geophys Res 73:3181–3205

Wright HMN, Cashman KV, Rossi M, Cioni R (2007) Breadcrust bombs as indicators of vulcanian eruption dynamics at Guagua Pichincha volcano, Ecuador. Bull Volcanol 69:281–300

Wright HMN, Cashman KV, Gottesfeld EH, Roberts JJ (2009) Pore structure of volcanic clasts: measurements of permeability and electrical conductivity. Earth Planet Sci Lett 280:93–104

Zandona A, Patzig C, Rüdinger B, Hochrein O, Deubener J (2019) TiO_2(B) nanocrystals in Ti-doped lithium aluminosilicate glasses. J Non-Cryst Solids: X 2:100025. https://doi.org/10.1016/j.nocx.2019.100025

Zhang YX, Xu ZJ, Liu Y (2003) Viscosity of hydrous rhyolitic melts inferred from kinetic experiments, and a new viscosity model. Am Mineral 88:1741–1752

Zhang C, Almeev RR, Hughes EC, Borisov A, Wolff E, Hofer HE, Botcharnikov RE, Koepke J (2018) Electron microprobe technique for the determination of iron oxidation state in silicate glasses. Am Mineral 103:1445–1454